Solar radiation energy on the Tibetan plateau

Nuozhen Gelsor

Master's Thesis

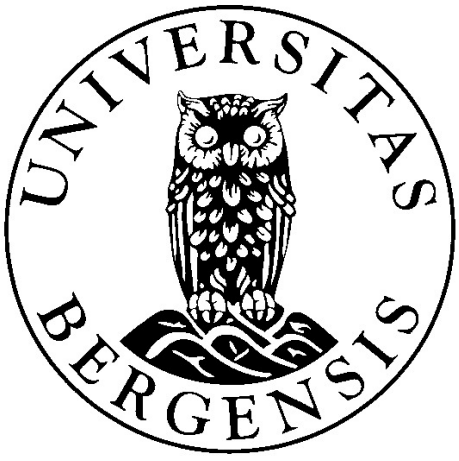

University of Bergen, Norway
Department of Physics and Technology
20th November 2015

Acknowledgements

This research was financed by the Norwegian Program for Development, Research and Education (Project code: PRO2007/10193N), the Network for University Cooperation Tibet-Norway (Environmental Physics in Tibet, Project code: 120112) and the Mt. Everest Scholar plan of Tibet University. My genuine gratitude goes to above mentioned programs and organizations, which made this research possible.

I'm very thankful for this opportunity to study in Norway for my master's degree. My education in Norway has been supported by many people. I would especially like to thank Professor Jakob J. Stamnes for his great help and kind encouragement.

My supervisor Børge Hamre is a brilliant, kind and lovable person. His passionate and patient guide truly supported me and my work during these years. I'm sincerely grateful for his great help. My deep gratitude goes to Ladislav Kocbach, the memorable nights sitting with him solving codes and exploring quantum mechanics will not be forgotten. I'm also thankful for Øyvind Frette, he did a great effort on helping me to adjust to this new environment. He vividly showed me the beauty of Norway and made me fall in love with this lovely country.

As a foreign student, it is not easy to write a thesis using a foreign language, therefore, I'm deeply thankful for Lucas Höppler. He kindly and patiently improved the linguistic and grammatical mistakes in this thesis, and truly provided a great help. In addition he has been very supportive and encouraging in this period.

Lastly, I want to thank my parents Norsang Gelsor and Drenma Tsering for my entire education and for their loving and caring for their only daughter, always.

Contents

Abstract

To gain a thorough knowledge of the solar energy resources on the Tibetan Plateau, measured and modeled solar irradiance levels on the Plateau from July 2010 to September 2013 are considered. The Tibetan Plateau lies in southwest China between 27.3 °N and 36.4 °N at an average altitude exceeding 4500 meters, where the amount of overhead atmosphere is reduced to almost one half of the amount at sea level. The combination of low solar zenith angles with low atmospheric attenuation and good weather gives high solar radiation levels, which could be exploited by solar power plants.

To quantify irradiance levels as well as their spatial and temporal variations, pyranometer measurements of the solar irradiance were recorded every minute throughout the years 2010 to 2013 in Lhasa (29.6 °N, 91.2 °E, 3683 m), Nagqu (31.5 °N, 92.1 °E, 4510 m), Tingri (28.7 °N, 87.1 °E, 4335 m), and Nyingchi (29.7 °N, 94.7 °E, 2995 m). The high irradiance values (around 1200 to 1300 W m^{-2}) at the Tibetan Plateau are found to be comparable with those at the Top of the Atmosphere (TOA) (1300 W m^{-2}). The yearly solar energy received by a horizontal surface is found to be about 7.6 GJ m^{-2} in Lhasa and 6.8 GJ m^{-2} in Nagchu. As expected, the highest irradiance values are observed at around 06:00 UTC (local noon), and the daily radiant exposure on a clear winter day is only about 54 % of that on a clear mid summer day. Based on the monthly averaged daily radiant exposure, Tingri has the best solar energy resource of the four sites and Nyingchi has the lowest. Lhasa has a richer solar energy resource than Nagchu.

A radiative transfer model (AccuRT (Hamre et al., 2014)) is used to examine the air quality by comparing modeled results with spectral radiometer measurements recorded during one day at two sites in mainland China and two sites in Tibet. The retrieved spectral transmittances show that the atmosphere above the two sites in Tibet is much more transparent than that above the sites in mainland China. Applying AccuRT, we also found out the weather has a more significant impact on the yearly radiant exposure (up to 23% variation between the four sites) than latitude (2% variation) or altitude (2% variation). Finally, sensitivity of irradiance levels due to variations in the aerosol and cloud optical depths were investigated. The yearly radiant exposure was reduced by aerosols by about 3% to 6% for typical aerosol optical depths in Tibet (0.17 - 0.27 at 580 nm). The combined effect of aerosols and clouds reduced the yearly radiant exposure by 15% in Lhasa and 23% in Nagchu. To cover the yearly power consumption in the Lhasa region, about 5.3 to 5.9 km^2 of horizontally oriented solar panels are necessary assuming a light-electricity transformation efficiency of 16% (Narbel et al., 2014) and a yearly radiant exposure of 7.6 and 6.8 GJ m^{-2}, respectively.

Chapter 1

Introduction

The upper atmosphere of the Earth receives an annual average of 174000 terawatts incoming solar radiation (Jaccard, 2006). Compared to the world power consumption of 13.5 terawatts in 2001 and 27 terawatts expected in 2050 (Lewis, Nathan, and Nocera, 2006), the incoming solar energy is significantly higher than the yearly world energy demand. Some of this huge amount of energy can be used to generate electricity by photovoltaic (PV) systems.

Since a PV system has a fast and non-linear response to the incident radiation levels (Suehrcke and McCormick, 1989), it is important to have temporal and spatial solar irradiance measurements to understand the fluctuating nature of the solar radiation and to get a realistic view of the possible output of PV systems. Such measurements are also essential to optimize the non-linear PV systems.

During the past years, solar energy conversion devices have gone through a qualitative progress: In 1888 Edward Weston received the first US patent for a "solar cell". In 1905, Albert Einstein published the theory of the "photoelectric effect" to explain the light-electricity transformation. In 1954, Bell Laboratories developed Si solar cells and achieved 6% light-electricity transformation efficiency applying silicon semiconductors. At that time, these solar cells were mainly used for satellites and they were adopted by Germany and Japan in the early 20 century. Nowadays, the typical solar panel is made of various materials and has an efficiency of about 16% (Narbel et al., 2014). Moreover, they are widespread in the market. As an example, Figure 1.1 shows a 10 MW PV power plant in Shigatse, Tibet. This area has a large solar energy resource with an average annual radiance exposure of 6 to 8 GJ m^{-2} (Wang and Qiu, 2009).

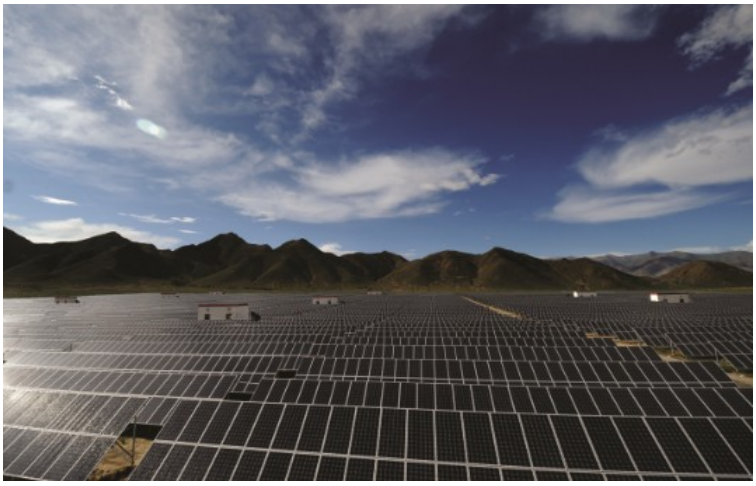

Figure 1.1: 10MW PV Power Plant in Shigatse, Tibet.
(Source: http://en.linuosp.com/dxdz/jpgc/1067.html, 2015)

The Tibetan Plateau is ranked as the richest solar energy resource in China, and after the Sahara, as the second richest solar energy resource worldwide (Wang and Qiu, 2009). There are two reasons for this. Firstly, Tibet lies between roughly 28 to 36 °N latitude. These low latitudes have high solar elevations and therefore high levels of radiation per area. Secondly, the average altitude of this highest and largest plateau in the world exceeds 4500 meters which makes the atmosphere thin and highly transparent for solar radiation.

Up to now, research on solar energy resources in Tibet has mainly been focused on UV radiation. In 1997, the first UV dose rates were calculated using data from a multi-channel moderate bandwidth filter instrument, which had been measured for five months from June 1996 to October (Ren et al., 1997). Ten years later, Dahlback et al. (2007) used data from a multichannel moderate-bandwidth UV filter instrument from NILU (Norwegian Institute for Air Research) to calculate the UV index in Lhasa during winter and summer 2003 (Dahlback et al., 2007). In 2009, the first long term measurements (three years) of UV radiation were taken in Lhasa from July 1999 to November 2002 (Norsang et al., 2009). In 2014, the UV index (UVI), the Total Ozone Column (TOC) and the Radiation Modification Factor (RMF) were compared at four sites on the Tibetan Plateau from July 2008 to September 2010 (Norsang et al., 2014).

Even though UV measurements are well covered on the Tibetan plateau, accurate solar irradiance measurements are not widely available due to high costs for equipment. Consequently, empirical models and estimations using climatological parameters are applied to estimate solar irradiance. To obtain daily radiant exposure at four sites in Tibet (Changdu, Geer, Lhasa, Nagqu), an estimation based only on sunshine duration measurements was carried out by Huashan Li using eight models (Li et al., 2011). Results showed that the Mean Percentage Error (MPE) for daily radiant exposure was between 1.7 and 7.4%. Tang et al. (2010) evaluated a hybrid model proposed by Yang et al. (2006) to calculate daily radiant exposure at 97 sites in China including three sites in Tibet. The Root Mean Square Error (RMSE) was less than 2.8 MJ m^{-2} for daily radiant exposure.

Publications of long-term solar irradiance measurements covering the whole solar spectrum are rare. From 2001 to 2005 observations were made for a site called Gaize on the Tibetan Plateau. The five year mean daily radiant exposure was found to be about 21 MJ m^{-2}, which is much higher than in other regions at similar latitudes (Liu et al., 2012). The solar global irradiance in Tibet (Lhasa) has also been occasionally monitored by the Tibet Meteorological Bureau (TMB) and the Chinese Academy of Science (CAS), but a systematic analysis has never been presented (personal communication with Professor Norsang Gelsor at the Tibet University).

The scarceness of a systematic study of long-term solar irradiance measurements in Tibet is the motivation for this thesis. In this thesis the following questions will be addressed.

- How does the solar irradiance vary temporally and spatially in Tibet?

- How is the irradiance transmittance of the atmosphere in Tibet compared to that in low-altitude regions and in aerosol loaded cities in mainland China?

- What is the maximum available annual solar energy in an optimistic and realistic scenario, and how does the weather conditions influence the solar irradiance in Tibet?

In Chapter 2, the theories used in this thesis are described. The instrumentation is presented in Chapter 3. The results including an analysis of spatial and temporal variations of the solar irradiance (310 - 2800 nm) as well as simulations performed with a Radiative Transfer model (AccuRT (Hamre et al., 2014)) in Tibet are described and discussed in Chapter 4. Finally, conclusions are drawn in Chapter 5.

Chapter 2

Theory

This chapter describes the theories applied in this thesis. Definitions are presented in subsection 2.1, and the theory of the radiative transfer model are presented in subsection 2.2.

2.1 Definitions

Irradiance:
Irradiance is defined as the total amount of solar energy (integrated over all directions and wavelengths) falling on a unit horizontal surface per second. The SI unit is watt per square meter [W m^{-2}].

Spectral irradiance:
Spectral irradiance is the irradiance per unit wavelength. It has the unit [W m^{-2} nm^{-1}].

Radiant exposure:
Radiant exposure is defined as the irradiance integrated over a certain period of time. It has the unit [J m^{-2}].

The daily radiant exposure is the irradiance integrated over one day. Similarly, monthly and yearly radiant exposure are the irradiance integrated over one month and one year, respectively.

Inherent optical properties:
The inherent optical properties (IOPs) are the absorption and scattering properties of a medium, IOPs do not change with angular distribution of the radiation. The scattering phase function describes the angular variation of the scattered radiation.

Yearly averaged Cloud Modification Factor (YCMF):
YCMF (dimensionless) describes how strongly clouds affect the yearly radiant exposure at a certain observation site. It is given by Eq. 2.1

$$\text{YCMF} = \frac{\text{Measured yearly radiant exposure}}{\text{Computed yearly radiant exposure (cloud and aerosol free atmosphere)}}. \tag{2.1}$$

Yearly averaged Aerosol Modification Factor (YAMF):
Similarly, the effect of aerosols on the yearly radiant exposure is given by

$$\text{YAMF} = \frac{\text{Yearly radiant exposure measured with aerosols (no clouds)}}{\text{Computed yearly radiant exposure (cloud and aerosol free atmosphere)}}. \tag{2.2}$$

2.2 Accurate Radiative Transfer model (AccuRT)

AccuRT is an easy-to-use radiative transfer simulation tool, which generates irradiances at user-specified locations (in an atmosphere-surface system) for given input parameters and user-specified IOPs (Hamre et al., 2014). In the atmosphere-surface system, AccuRT supports an arbitrary number of layers (from 0 to 100 km) to resolve vertical variations in the IOPs. The knowledge of the IOPs of each atmospheric component in each layer is critical.

When electromagnetic radiation penetrates from the top of the Earth's atmosphere towards the surface, light-matter interactions (attenuation) occur. There are two forms of light-matter interactions: absorption and scattering. Each of them corresponds to an absorption coefficient and a scattering coefficient. The absorption coefficient $\alpha(z)$ and the scattering coefficient $\beta(z)$ are defined as:

$$\alpha(z) = \frac{1}{I^i}\left(\frac{dI^\alpha}{dz}\right) \tag{2.3}$$

$$\beta(z) = \frac{1}{I^i}\left(\frac{dI^\beta}{dz}\right). \tag{2.4}$$

I^i is the incident radiance entering a volume element $dV = dAdz$ with the cross sectional area dA and the propagation distance dz. dI^α and dI^β are the radiances that are absorbed and scattered in all directions as the light propagates a distance dz along the direction $\hat{\Omega}'$ within the volume element dV. The single-scattering albedo given by

$$a(z) = \frac{\beta(z)}{\alpha(z) + \beta(z)}, \tag{2.5}$$

which represents the radiation loss caused by scattering. It is the portion of the attenuated light due to scattering.

2.2.1 Attenuation due to molecules

When sunlight interacts with molecules of gases, two attenuation processes can occur: Rayleigh scattering and molecular absorption.

Molecular scattering (Rayleigh scattering)

Rayleigh scattering, is the scattering process in which sunlight is scattered by particles that are much smaller than the wavelength λ of the radiation (diameter $< \lambda/10$). The scattered light is inversely proportional to the fourth power of the wavelength of light, which means that the shorter the wavelength, the more light will be scattered, i.e.

$$I \propto \frac{1}{\lambda^4}. \tag{2.6}$$

The angular distribution of the scattered light (after a single scattering event) is given by the scattering phase function P(cosΘ), which is a dimensionless quantity that can be described as (Thomas and Stamnes, 1999; Stamnes and Stamnes, 2015):

$$\mathrm{P}(\cos\Theta) = 4\pi \frac{\beta_{\mathrm{v}}(\cos\Theta)}{\int_{4\pi} \beta_{\mathrm{v}}(\cos\Theta)\mathrm{d}\omega} = \frac{\beta_{\mathrm{v}}(\cos\Theta)}{\frac{1}{2}\int_{-1}^{1} \beta_{\mathrm{v}}(\cos\Theta)\mathrm{d}(\cos\Theta)} \tag{2.7}$$

where $\beta_{\mathrm{v}}(\cos\Theta)$ is the volume scattering function, defined as the ratio of the radiance of the scattered light per solid angle to the incoming light times the propagation distance dz of the volume element. The unit of β_{v} then becomes $\mathrm{sr}^{-1}\mathrm{m}^{-1}$. The integration of the volume scattering function over all angles gives the scattering coefficient, i.e. $\int_{4\pi} \beta_{\mathrm{v}}(\cos\Theta)\mathrm{d}\omega = \beta(\mathrm{z})$, so that

$$\frac{1}{4\pi}\int_{4\pi} P(cos\Theta)d\omega = 1, \tag{2.8}$$

where Θ is the scattering angle between the direction of the incident and the scattered radiation. $(1/4\pi)P(cos\Theta)$ is the probability that a light beam traveling in the direction $\hat{\Omega}'$ is scattered into a cone of solid angle $\mathrm{d}\omega$ around the direction $\hat{\Omega}$ within the volume element dV with thickness dz along $\hat{\Omega}'$.

For Rayleigh scattering, the scattering phase function is given by:

$$P(cos\Theta) = \frac{3}{4}(1 + cos^2\Theta). \tag{2.9}$$

Molecular absorption

In the atmosphere, the main absorbers of solar radiation are ozone and water vapor. A small amount of absorption is also caused by oxygen and carbon dioxide.

The ozone layer is located around 10 to 50 km above the Earth's surface and is mostly produced by ultraviolet (UV) radiation (in the UVC band) and X-rays. Therefore, ozone efficiently absorbs UV radiation and X-rays. The absorption cross section increases rapidly below (roughly) 320 nm. Ozone is also the main absorber in the visible spectrum (Gorshelev et al., 2014).

Water vapor, mainly located in the troposphere (below 10 km), absorbs particularly within the long wave band of the solar radiation spectrum. Oxygen heavily absorbs the light around 759 nm (Fraunhofer's A line).

2.2.2 Attenuation due to aerosols

Aerosol absorption

Aerosols are airborne solid or liquid particles. The particle sizes can range from a few nanometers (fine mode) to more than ten micrometers (coarse mode). Absorption becomes important for Black Carbon (BC) aerosols. A significant amount of light can also be absorbed by brown carbon and mineral dust. These aerosols are introduced into the atmosphere by biomass burning, combustion processes, and dust entrainment. Absorption is proportional to the particle volume and to the mass for particles that are much smaller than the wavelength of the incident light (Moosmüller et al., 2009).

Aerosol and cloud scattering

In the atmosphere, aerosols are often observed as dust, fog or cloud particles, which are located in the lower atmosphere. Cloud particles are larger than the wavelength of the incident light, and scatter solar radiation at all wavelengths similarly (Mie scattering).

For a typical size distribution, aerosols that have sizes comparable to the wavelength of the incidence light, scatter light more efficiently. However, the shorter the wavelength, the more light can be scattered if the aerosol sizes are smaller than the wavelength. The wavelength dependence of aerosol scattering is often about inversely proportional to the wavelength. Therefore, in addition to Rayleigh scattering, small aerosols will scatter more light at short wavelengths.

In AccuRT, aerosols are modeled as spheres, and the Henyey-Greenstein (HG) scattering phase function (Henyey and Greenstein, 1941) can be applied as an approximation to the scattering phase function for scatterers with sizes comparable to or larger than the wavelength:

$$P(\cos\Theta) = \frac{1 - \mathrm{g}^2}{(1 + \mathrm{g}^2 - 2\mathrm{g}\cos\Theta)^{\frac{3}{2}}}. \tag{2.10}$$

Where g is called the asymmetry factor, which is calculated by averaging the cosine of the scattering angle over all directions (weighted by $P(\cos\Theta)$).

$$g =< \cos\Theta >= \frac{1}{4\pi} \int_{4\pi} \mathrm{P}(\cos\Theta)\cos\Theta \mathrm{d}\omega, \tag{2.11}$$

where $g > 0$ means that most of the incident light is scattered in the forward direction ($\Theta < \pi/2$), $g < 0$ means that most of the light is scattered in the backward direction ($\Theta > \pi/2$), and $g = 0$ represents isotropic scattering or symmetric scattering. $g = 1$ represents complete forward scattering, and $g = -1$ represents complete backward scattering.

2.2.3 Radiative Transfer Equation (RTE)

AccuRT computes radiances by solving the Radiative Transfer Equation (RTE) for each layer of the atmosphere-surface system and at any location for given IOPs. As a premise, the atmosphere is treated as a vertically stratified medium which is in local thermodynamic equilibrium. The diffuse radiance $\mathrm{I}_{diff}(\tau, \hat{\Omega})$ is expressed by the RTE:

$$\mu \frac{dI_{diff}(\tau, \hat{\Omega})}{d\tau} = I_{diff}(\tau, \hat{\Omega}) - S^*(\tau, \hat{\Omega}) - \frac{a(\tau)}{4\pi} \int_{4\pi} P(\tau, \hat{\Omega}'; \hat{\Omega}) I_{diff}(\tau, \hat{\Omega}') d\omega'. \tag{2.12}$$

Here μ is the cosine of the polar angle θ. $\hat{\Omega}'$ is a unit vector representing the direction of an incoming light beam before scattering. $\hat{\Omega}$ is a unit vector indicating the direction of the scattered light. $a(\tau)$ is the single-scattering albedo (see Eq. 2.5).

The term on the left side of the equation indicates the rate of change of the diffuse radiation in direction $\hat{\Omega}$ with optical depth τ. $\mathrm{I}_{diff}(\tau, \hat{\Omega})$ is the diffuse light that is scattered into the direction $\hat{\Omega}$. $S^*(\tau, \hat{\Omega})$ is a "source" term, which generates the diffuse radiation field. Without it, there will be no diffuse light. And $\mathrm{P}(\tau, \hat{\Omega}'; \hat{\Omega})$ is the scattering phase function which indicates the probability of one beam coming from direction $\hat{\Omega}'$ is scattered into direction $\hat{\Omega}$. After multiplying the diffuse radiance with the scattering phase

function and integrating it over all incoming directions $\hat{\Omega}'$, the total scattered light into the direction $\hat{\Omega}$ (last term on the right side) is obtained. The differential vertical optical depth is

$$d\tau(z) = -(\alpha(z) + \beta(z))dz. \tag{2.13}$$

Here z increases in the upward direction, therefore, Eq. 2.13 indicates that τ decreases in the upward direction.

AccuRT calculates the irradiance on the Earth's surface as follows:

(i) Separate the atmosphere into a sufficiently large number of homogenous horizontal layers, in each of which the optical properties remain constant.

(ii) Discrete-ordinate solutions to the RTE are obtained by converting the integro-differential RTE into a system of coupled ordinary differential equations for each layer.

(iii) At the Top of Atmoshpere (TOA) and at the surface, boundary conditions are applied.

2.2.4 Scaling factor

Since at the altitude of the Tibet Plateau the amount of air molecules is reduced, a scaling factor is necessary to reduce the thickness of the atmosphere to an appropriate value. A scaling factor of 0.9 for oxygen means that 90% of the oxygen column in the "US-standard" atmosphere is applied. The scaling factor k is calculated as follows:

In the atmosphere, the number of molecules per volume integrated from a certain altitude to the TOA is less than the number of molecules integrated from sea level to the TOA by a factor of k. This can be expressed as:

$$\int_h^\infty n(z)dz = k \int_{z_0}^\infty n(z)dz, \tag{2.14}$$

where z_0 is the sea level height and h is the altitude of a site in Tibet, and $n(z)$ is number of molecules per volume.

Thomas and Stamnes (1999) assumed an exponential decrease with height of the amount of molecules in the atmosphere, which is expressed by Eq. 2.15 below. In order to obtain this equation, the temperature variation is set to be constant from sea level to the height of the Tibetan Plateau. (Otherwise, the surface temperature of Lhasa would be negative during summer, which is not the case.)

$$n(z) \approx e^{-\frac{z-z_0}{H}} n(z_0), \tag{2.15}$$

H is the atmospheric scale height, at which the density of the atmosphere is reduced by a factor of 1/e. Inserting Eq. 2.15 into Eq. 2.14, we find:

$$\int_h^\infty e^{-\frac{z-z_0}{H}} n(z_0)dz = k \int_{z_0}^\infty e^{-\frac{z-z_0}{H}} n(z_0)dz. \tag{2.16}$$

Since z_0 represents the sea level height, which is at 0 m, we have:

$$\int_h^\infty e^{-\frac{z}{H}} n(z_0)dz = k \int_0^\infty e^{-\frac{z}{H}} n(z_0)dz. \tag{2.17}$$

Since $n(z_0)$ is the number of molecules per volume on the sea level, which is a constant, we obtain:

$$\int_h^\infty e^{-\frac{z}{H}} dz = k \int_0^\infty e^{-\frac{z}{H}} dz. \tag{2.18}$$

By solving Eq. 2.18 the scaling factor k is obtained:

$$k = e^{\frac{-h}{H}}, \tag{2.19}$$

where $H = (1/29.3)T$ and T is the local temperature in Kelvin. k is 0.64 for Lhasa and 0.62 for Nagchu, which have annual mean temperatures of 9.4 °C (282.6 K) and 0 °C (273.2 K), respectively.

2.2.5 Gaussian smoothing

Gaussian smoothing is applied in order to compare computed high-resolution spectra to the spectra measured with a Ramses sensor (see subsection 3.3), which has a spectral resolution of 10 nm.

The Gaussian filter is plotted in Figure 2.1, while the corresponding equation is expressed by the following formula:

$$E(\lambda) = \frac{1}{\sigma\sqrt{2\pi}} e^{-\frac{(\lambda-\lambda_0)^2}{2\sigma^2}}, \tag{2.20}$$

where λ_0 is the average value and σ is the standard deviation. The relationship between the Full Width Half Maximum (FWHM) and the standard deviation is FWHM $\approx 2.36\sigma$.

The standard deviation of 4.25 is applied since the FWHM of Ramses sensor is 10 nm.

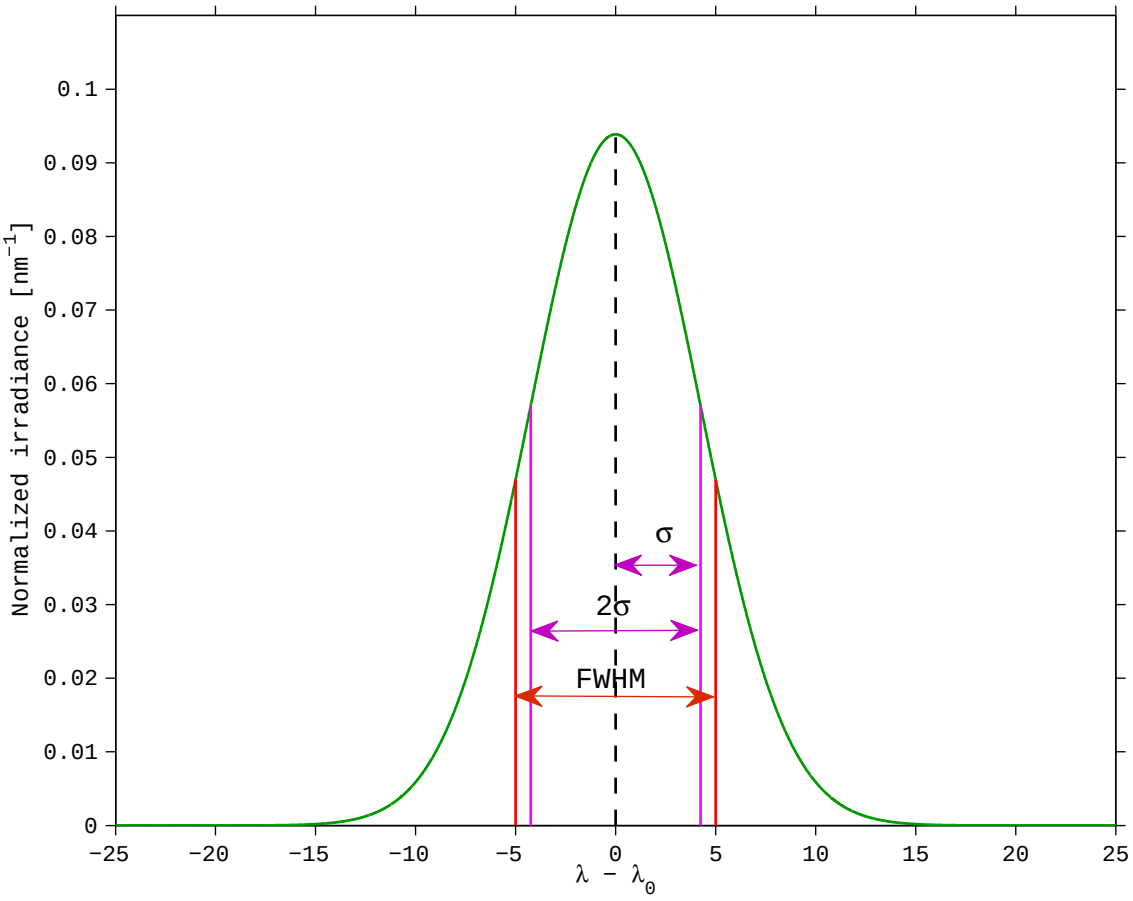

Figure 2.1: Normalized Gaussian filter, $\sigma = 4.25$.

Chapter 3

Instrumentation

3.1 Introduction of the measurement sites in Tibet

The Tibetan Plateau lies between the Himalayan range in the south and the Kunlun Range in the north. With a total area of about 2.3 million square kilometers, the Tibetan Plateau possesses several of the world's highest mountains and is the source of several major rivers, including the Yellow river, which in Chinese has the name *Mother River*. The Tibetan Plateau impacts the climate and the ecosystems of the Asian continent and also, the whole world. Research has shown that the uplift of the Himalaya Tibetan plateau is the primary driving force of Asian monsoons (Zhisheng et al., 2001). Moreover, high mountain chains influence the kinetic energy of stationary and transient disturbances in the atmosphere (Manabe and Terpstra, 1974).

The solar irradiance measurements are conducted on the Tibet side of the Himalaya range (the snow covered mountain chain in Figure 3.1). Four pyranometers were mounted at four sites in Tibet, namely, Lhasa, Nagchu, Tingri and Nyingchi (marked as yellow dots in Figure 3.1).

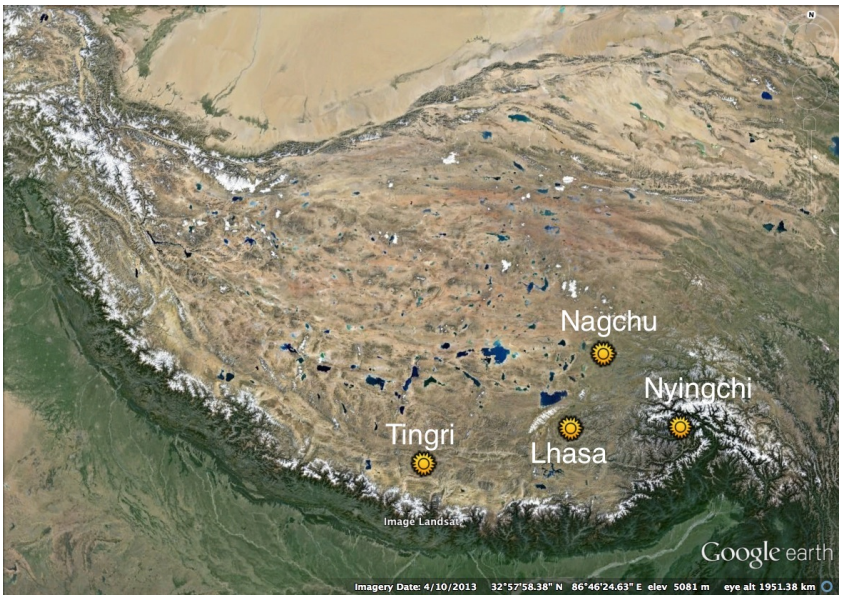

Figure 3.1: Measurement sites (yellow dots) in the Himalayan mountain region. Map data: Google, Landsat.

We have used TuTiempo.net, which has historical weather records for over 8000 weather stations worldwide, to retrieve extreme temperatures and the annual mean temperatures for all four sites.

3.1.1 Lhasa, Tibet

Lhasa, lies in the southeast of Tibet, and is the centre of economics, religions and politics in Tibet. *Kyi chu* (Lhasa river) passes through the south part of Lhasa, and the whole city is surrounded by high mountains (Figure 3.2a). The solar irradiance measurements are recorded at the new campus of the Tibetan University in Lhasa. The university is located in the southeast of the city and the mountains which are near to the campus are about six hundred meters above the altitude of Lhasa. The distances from the observation site to the surrounding highest mountains are also displayed in Figure 3.2a. Moreover, the valley landform protects Lhasa from extreme temperatures as well as strong winds. Due to the high altitude, averaging 3600 m, Lhasa generally has a dry and cool semi-arid climate with about 500 mm annual rainfall (Norsang et al., 2014). The climate in Lhasa is mild, with an annual averaged temperature of about 9.4 °C which increases every decade by about 0.16 °C (Liu and Chen, 2000). The minimum and maximum monthly average temperatures are about 0.9 °C in January and 17.0 °C in July. Extreme temperatures can reach -11 °C in winter and 27 °C in summer.

Figure 3.2b shows a pyranometer mounted on the top of the Physics building at Tibet University, having a great view of the sky. Lhasa has about 3000 sunshine hours per year. Solar irradiance values were measured in Lhasa from July 2010 to September 2012.

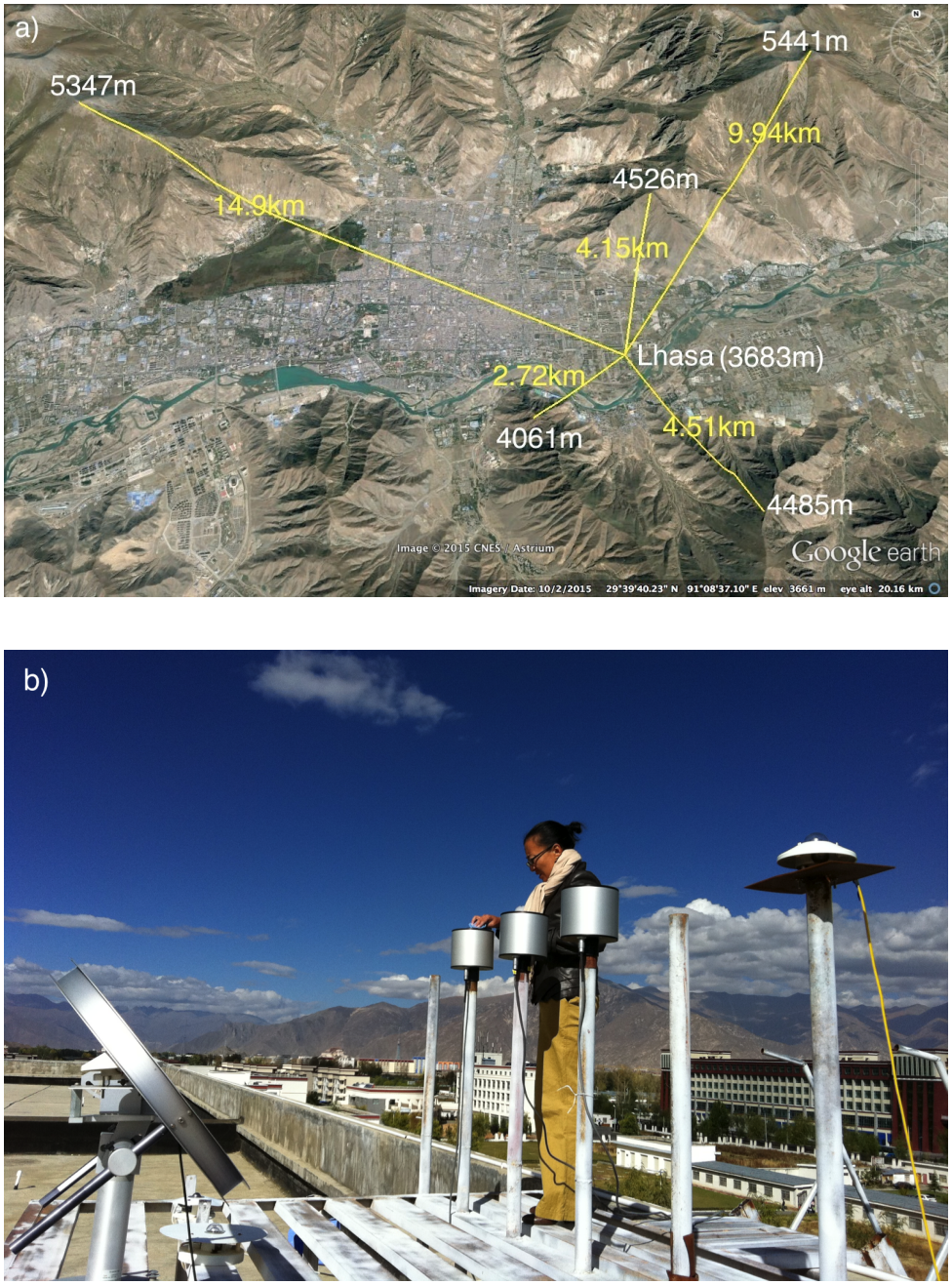

Figure 3.2: (a): Satellite picture of the instrument location in Lhasa and the distances from the instrument to the mountains nearby. (Google Earth image taken on 02/10/2015. Map data: Centre National d'Etudes Spatiales (CNES) 2015 distribution Astrium services, spot image.) (b): Instruments mounted at Tibet University in Lhasa: three NILU UV radiometers acquires UV measurements are placed close to the pyranometer. On the left side of the figure, a pyranometer with a shadow band is placed to detect diffuse light. Source: Norsang Gelsor, 2013.

3.1.2 Nagchu, Tibet

Nagchu town is located in the Nagchu prefecture in Northern Tibet, which is covered mostly by grass land and small hills, with few high mountains. It ranges from 83.5 °E to 95.16 °E and from 30.5 °N to 35.6 °N, and the total land area is around 446000 square kilometers. As the highest portion of the Tibetan Plateau, Northern Tibet plays an important role in water supply and stock-breeding. The climate of Northern Tibet is predominantly very cold and dry, due to the sub-frigid, semi-arid and monsoon climate. The average annual precipitation is between 247 and 514 mm (Gao et al., 2009). According to Gao et al,. (2009), in 33% of the area in Northern Tibet, the precipitation contributes positively to a Net Primary Productivity (NPP: the production of chemical energy in organic compounds by living organisms) in recent years. This result can be due to the resulting moist land which is suitable for plants to grow. In contrast, in 37% of the area in Northern Tibet, the total solar radiation contributes negatively to the NPP, possibly due to dry earth. Therefore, Nagchu town was chosen as an observation site. The solar irradiance measurements in Nagchu provide a great opportunity to explore the climate in Northern Tibet, including grass and livestock productivity.

Nagchu has an annual average temperature of around 0 °C in recent years (increasing 0.16 °C every decade (Liu and Chen, 2000)). The temperatures of the warmest days in Nagchu can increase to 20 °C and decline to about -25 °C for the coldest days. Despite of a harsh and alpine climate with long and cold winters, and short summers, Nagchu still receives 2866 sunshine hours per year, and an average annual rainfall of 380 millimeters (Norsang et al., 2014).

Figure 3.3a shows a map of Nagchu. The pyranometer was installed almost at the centre of the city. The closest mountain top (4660 m) is about 2.9 km away from the instrument. The distances from the observation site to the nearby mountains are also marked in Figure 3.3a. Figure 3.3b shows that the pyranometer was set next to a NILU instrument, the pyranometer recorded solar irradiance every minute from July 2010 to September 2013. Since there are no high mountains around Nagchu (unlike Lhasa), the sunlight is rarely blocked or influenced by reflection.

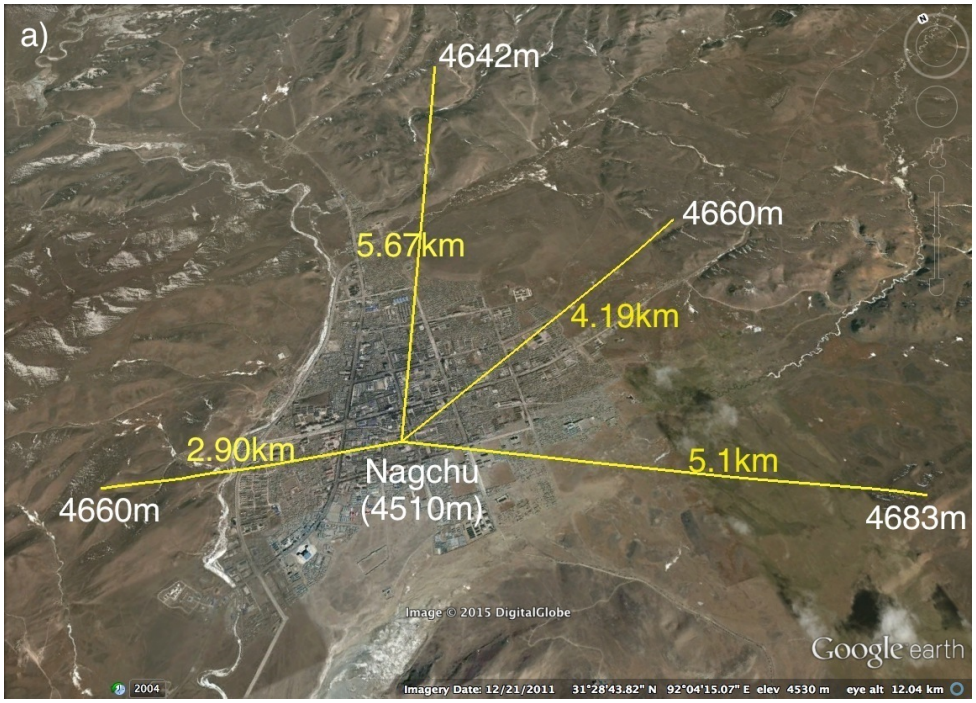

Figure 3.3: (a): Satellite picture of the instrument location in Nagchu and the distances from the instrument to the mountains nearby. (Google Earth image taken on 21/12/2011. Map data: Google, DigitalGlobe.) (b): Instruments mounted in Nagchu site: a NILU UV radiometer and a pyranometer are mounted next to each other, the NILU instrument records UV measurements and the pyranometer recording broad-band irradiance data. Source: Norsang Gelsor, 2013.

3.1.3 Tingri, Tibet

Tingri lies next to the south boarder of Tibet and shares Mt. Everest with Nepal. Mt. Everest can often be seen from the Tingri site. Figure 3.4 is taken from the road towards Tingri, the direct distance between Mt. Everest and Tingri is only around 60 km (annotated in Figure 3.4). The solar irradiance at Mt. Everest affects various climatic factors, such as ice and snow coverage and precipitation. The glaciers upon the high Asia Mountains can indicate climate change sensitively and record variations in atmospheric processes (Kang et al., 2002). Such information is obtained by analyzing the major ions in the deep ice core. The analysis shows the regions these ions come from and the atmospheric circulation that has transported them, for example winter atmospheric circulation or summer atmospheric circulation.

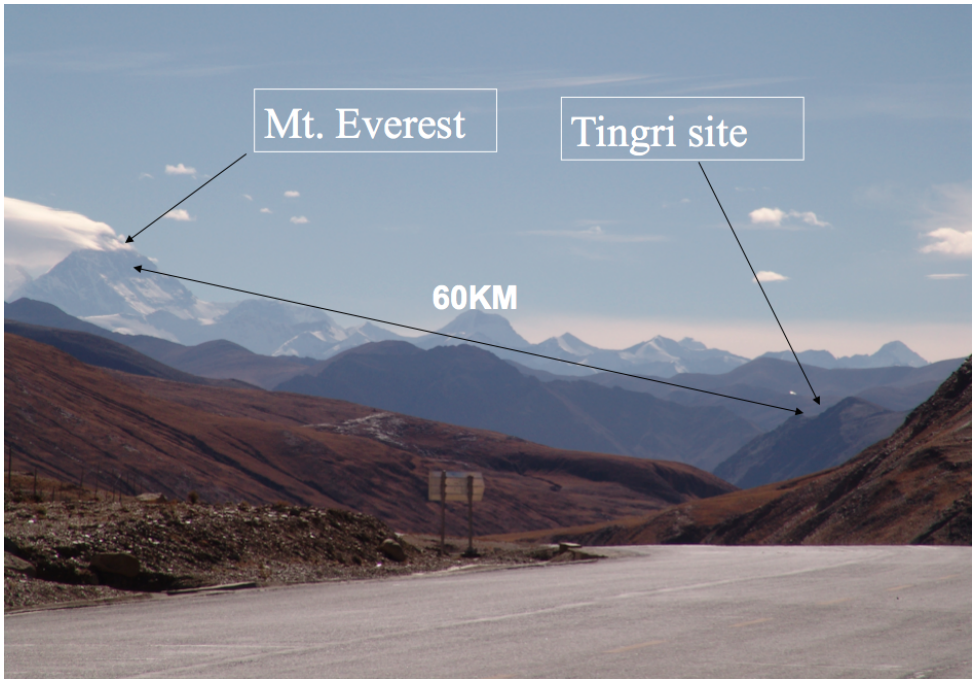

Figure 3.4: Mt. Everest and Tingri site. Source: Norsang Gelsor, 2013.

The map in Figure 3.5a of Tingri shows several relatively bright mountains surrounding our instruments and again the geographical distance is marked.

In Figure 3.5b, the Pyronameter in Tingri was mounted in the field together with two NILU instruments, having a wide view of the sky. The semi-arid climate is obvious in Figure 3.5b. This Pyronameter recorded solar irradiance in Tingri from July 2010 to the end of 2012.

Tingri is located in the semi-arid monsoon climate zone with an annual mean temperature of about 4 °C. The extreme temperatures in Tingri can fall to -21 °C and increase to 23 °C. The highest precipitation fall in July and August, and the average annual rainfall is about 270 millimeters (Norsang et al., 2014). Snow falls between the end of October and the end of April and the maximum snowfall occurs in December, January and February. Snow is covering mountains for months, but is staying on the ground in Tingri only for

days (Norsang et al., 2014). The Pyronameter mounted in Tingri measured irradiance first for half a year starting from July 2010, and then for about seven months, starting from April 2012.

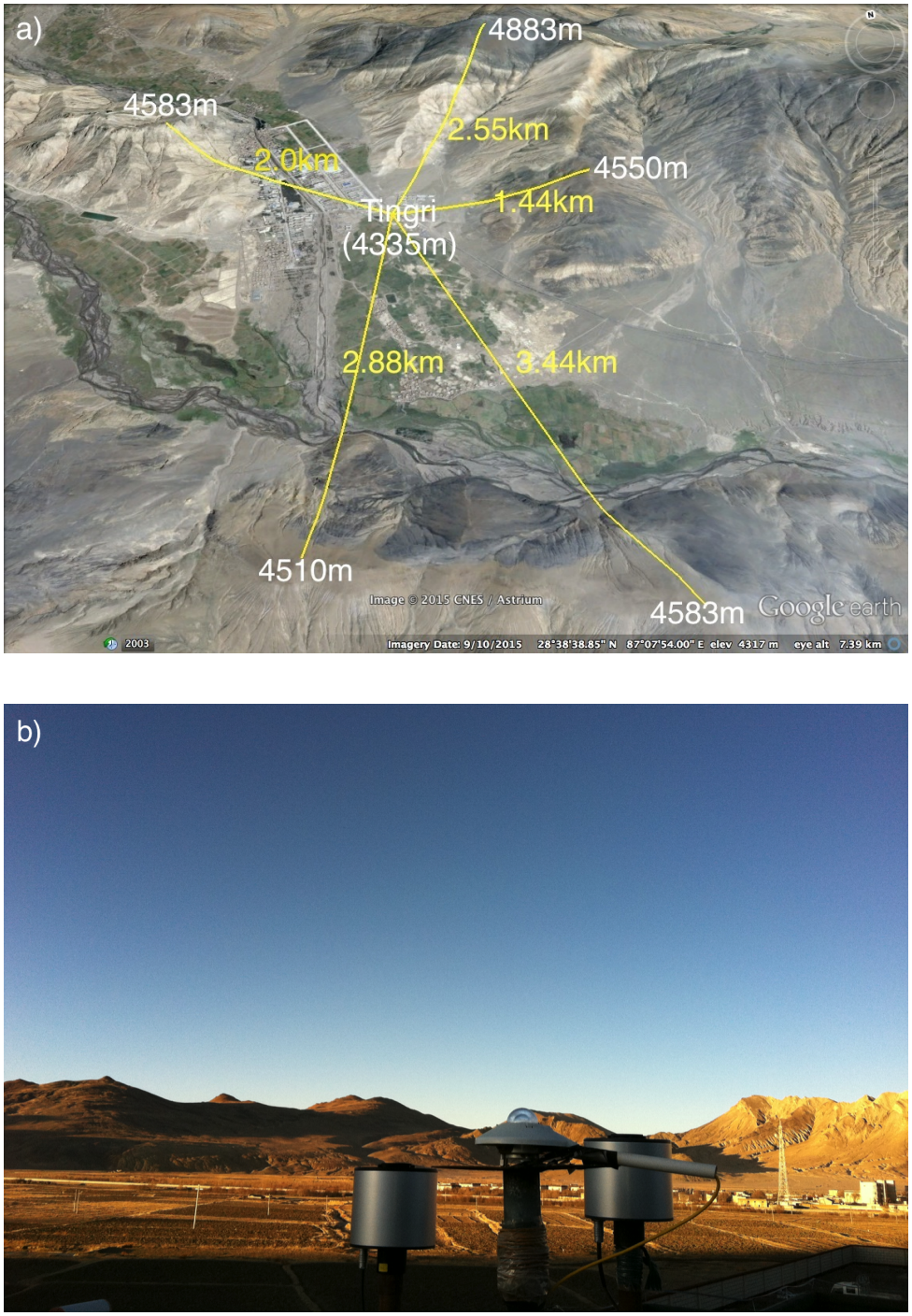

Figure 3.5: (a): Satellite picture of the instrument location in Tingri and the distances from the instrument to the mountains nearby. (Google Earth image taken on 10/09/2015. Map data: CNES 2015 distribution Astrium services spot image.) (b): Instruments at the Tingri site: two NILU UV radiometers and a pyranometer are mounted together to record UV measurements and broad-band irradiance data, respectively. Source: Norsang Gelsor, 2013.

3.1.4 Nyingchi, Tibet

Nyingchi is the lowest and easternmost site. The observation site is about 30 km away from the Brahmaputra river. The Northern Himalaya Mountains and Nyenchen Tanglha Mountains form the valley landform of Nyingchi. In Figure 3.6a, a rather low surface albedo is observed on 13th January in Nyingchi, and the distances from the instrument to the nearest high mountain peaks are marked.

Similar to Lhasa, Nyingchi is protected from extreme weathers. Due to the warm winds from India, this site has a semi-humid monsoon climate. The annual mean temperature is 10 °C with the hottest temperatures about 28 °C. The sunshine hours reach about 2022 and the average annual rainfall is 650 mm. It seldomly snows in Nyingchi (Norsang et al., 2014).

The Pyronameter in Nyingchi was mounted on the top of a building together with a NILU UV radiometer (Figure 3.6b). The broad-band solar irradiance was measured for half year in Nyingchi starting from July 2010.

The geographical information for the four sites are summarized in Table 3.1:

Table 3.1: Site informations.

Site	Instrument	Latitude [°N]	Longitude [°E]	Altitude [m]	Starting Date
Lhasa	Pyranometer	29.65	91.18	3683	Jul. 02, 2010
Nagqu	Pyranometer	31.47	92.06	4510	Jul. 02, 2010
Tingri	Pyranometer	28.66	87.13	4335	Jul. 10, 2010
Nyingchi	Pyranometer	29.66	94.37	2995	Jul. 02, 2010

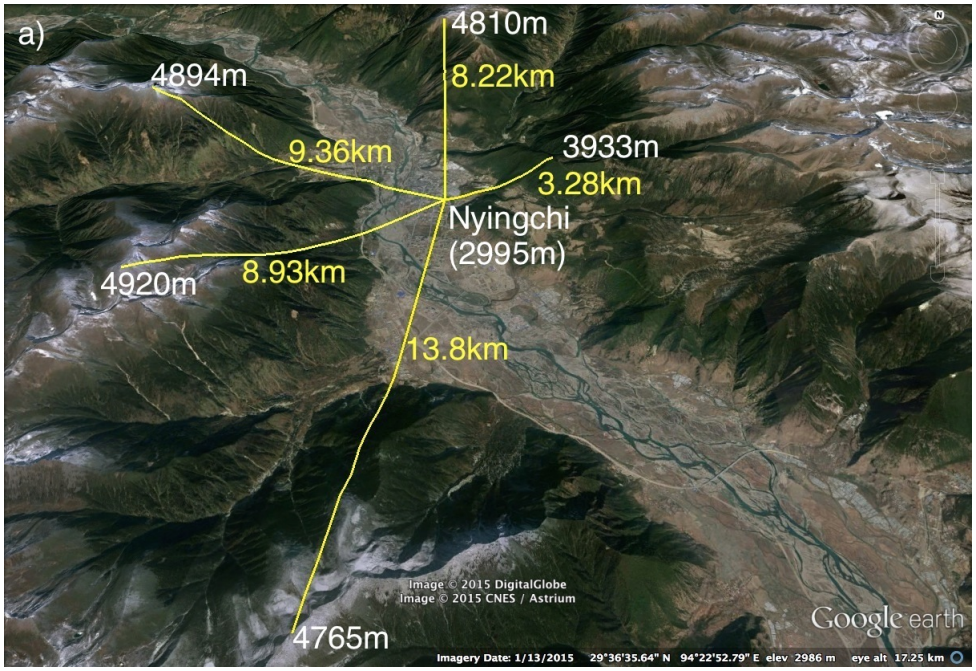

Figure 3.6: (a): Satellite picture of the instrument location in Nyingchi and the distances from the instrument to the mountains nearby. (Google Earth image taken on 13/01/2015. Map data: Google, DigitalGlobe and CNES 2015 distribution Astrium services spot image.) (b): Instruments at the Nyingchi site: a NILU UV radiometer and a pyranometer are mounted together to record UV measurements and broad-band irradiance data, respectively. Source: Norsang Gelsor, 2013.

3.2 Pyranometer CMP-6

Four thermopile Pyranometers (CMP-6) produced by Kipp & Zonen were applied in this thesis to measure the hemispherical broadband solar irradiance (W m^{-2}) in Lhasa, Nagqu, Tingri, and Nyingchi. Figure 3.7 shows the Pyranometer (CMP-6) in Lhasa.

Figure 3.7: Pyranometer CMP-6 at Tibet University. Source: Norsang Gelsor, 2013.

Most of the information in this subsection is obtained from the Kipp & Zonen Pyranometer Instruction Manual (KippZonen, 2013) and the Kipp & Zonen official website (http://www.kippzonen.com, 2015).

The CMP-6 Pyranometer uses the thermoelectric detection principle and has a blackened horizontal surface to absorb more than 97% of incoming radiation over a wide wavelength range. The corresponding temperature increase is sensed by thermocouples connected in series, thus forming a thermopile.

The thermopile sensing element is assembled by a large number of thermocouple junction pairs connected in series. The active (hot) junctions are attached under the blackened absorbing surface and heated by the incoming radiation. The reference (cold) junctions of the thermopile are thermally attached with the pyranometer housing, which serves as a heat-sink. In this way, the cold junctions are kept at a fixed temperature. The temperature difference between the active junctions and the reference junctions produce an electromotive force proportional to the temperature difference (Thermoelectric effect). More recently, for better performance, the dissimilar metals of a thermopile are replaced by dissimilar semiconductors (Peltier elements).

Double domes on the top are used to provide a better stability under dynamically changing temperatures and wind. It protects the sensor also from outer contaminative matter,

which at the same time limits the spectral sensitivity of thermopile-based instruments to 290 to 2800 nm (Badescu, 2008). The CMP-6 does not require a power supply. Data are recorded by LOGBOX SD with low power consumption, a small battery is contained in it. The detector generates 10 μV per W m^{-2}, which corresponds to around 10 mV on a sunny day. Measurements are recored every minute as 1 minute averages.

Ideally, the site for the radiometer should be as flat as possible and free of any objects above the detecting sensor. However, all selected sites in Tibet are surrounded by high mountain chains except Nagchu. However, all pyranometers were mounted on the top of high buildings having the best possible views of the sky. Errors due to the shadowing of the surrounded mountains are not corrected in the irradiance measurements presented in Chapter 4. A correction, which could be needed when comparing with plane parallel radiative transfer models, would possibly slightly increase the total irradiance. No special orientation of the instrument is required and the thermal-pile is horizontal within 0.1 ° after the leveling procedure.

The measured irradiance is calculated by integrating the cosine of the incoming beam from all directions. If the beam of light enters the atmosphere with a high zenith angle (the angle between the normal of the surface and the incoming radiance), the light projected on the horizontal surface will be spread over a large area. In this case, the amount of energy hitting the detector will be weaker (Lambert's cosine law). This is shown in Figure 3.8. In addition to mountain shadowing error, a possible error source comes from the non-perfect cosine response of a horizontal detector on a relatively high radiation zenith angle.

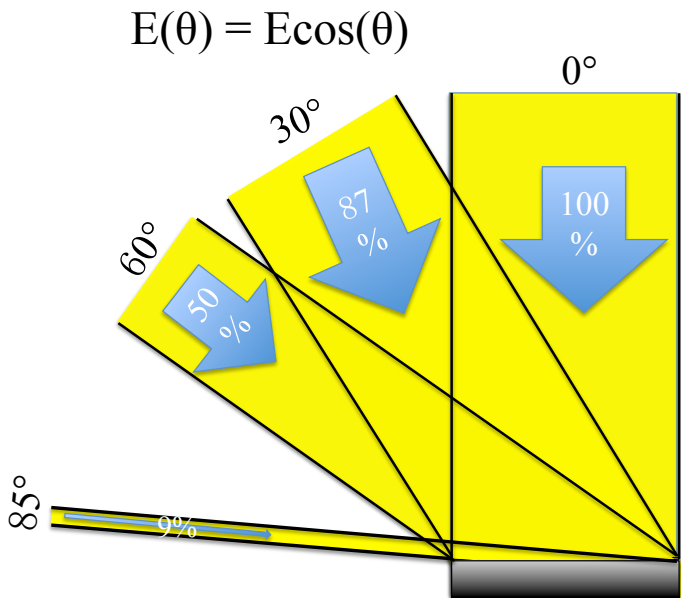

Figure 3.8: Lambert's cosine law.

3.2.1 Physical properties

The thermopile-based detectors are sensitive to the whole shortwave spectrum. The sensitivity of a pyranometer depends on both the individual physical properties of the thermopile and on the construction. The Zero offset A is below 15 W m^{-2} and it refers to a small negative output signal which is introduced by the heat exchange between the pyranometer domes and the relatively cold atmosphere. This effect can be minimized by using an inner dome as a "radiation buffer" and applying a ventilation unit. Zero offset B is proportional to the ambient temperature, but usually below 4 W m^{-2}. This causes instrument temperature variation and produces heat currents inside the radiometer. The directional error is the maximum deviation from the ideal cosine-response of the pyranometer and is below 20 W m^{-2}. The daily uncertainty is 5%, but the hourly uncertainty can be higher because some response variations cancel each other if the average period is long. The sensitivity of each thermopile is unique and, therefore, each radiometer has a unique calibration factor. All four pyronameters were calibrated by Kipp & Zonen before delivery, and then calibrated again every two years. The Pyranometer CMP-6 specifications are summarized in Table 3.2.

Table 3.2: CMP-6 performance specifications.

Specification	Unit	Value	Comments
Spectral range	nm	310 - 2800	
Sensitivity	μ V $W^{-1}{\cdot}m^{-2}$	5 to 20	signal for 1 W m^{-2} irradiance
Response time	S	< 18	95% of final value
Temperature dependence of sensitivity	%	< 4	variation in range -10 $°C$ to + 40 $°C$
Zero offset A	W m^{-2}	< 15	at 0 to -200 W m^{-2} of IR net radiation
Zero offset B	W m^{-2}	< 4	at 5 K/h temperature change rate
Operating temperature	°C	-40 to +80	storage temperature is the same
Field of view	°	180	hemispherical
Directional error	W m^{-2}	< 20	up to 80 ° with 1000 W m^{-2} irradiance
Maximum irradiance	W m^{-2}	2000	level above which damage may occur
Uncertainty in daily total	%	< 5	95% confidence level

3.3 Ramses-ACC-VIS and Ramses-ACC-UV

TriOS Ramses-ACC-VIS and Ramses-ACC-UV measure the spectral irradiance W m^{-2} nm^{-1} of visible (320 - 950 nm) and of UV light (280 nm - 500 nm). In this thesis, these spectral radiometers were applied in Lhasa and Shegatse in Tibet and in Chengdu and Beijing in mainland China. The instrument specifications in this subsection is a summary of what can be found in TriOS official website (http://www.Trios.de, 2015).

TriOS RAMSES-ACC-VIS and Ramses-ACC-UV (shown in Figure 3.9) are hyperspectral radiometers for the Visible (VIS) and UV spectral ranges. They have very low power consumption and, therefore, are convenient to apply in the field. The TriOS Ramses-ACC-VIS and Ramses-ACC-UV detectors use a white cosine collector made of fused silica, placed on the top of the instrument to diffuse the light into the optical fiber behind it. The output of the irradiance sensors is given as the incident power on a unit surface per wavelength. Each channel has a bandwidth of about 10 nm Full Width at Half Maximum (FWHM). Moreover, the sampling interval can be selected by user.

Figure 3.9: TriOS Ramses-ACC-VIS and Ramses-ACC-UV in Tibet University, Lhasa.

The detector type is a 256 channel silicon photo-diode array. The spectral accuracy is 0.3 nm for the RAMSES-ACC-VIS, which means that the uncertainty of the detected wavelength is about ±0.3 nm; the uncertainty for RAMSES-ACC-UV is ±0.2 nm. The longest exposure time for both radiometers is about 4 seconds. A relative calibration lamp (FieldCAL) is applied to correct for possible instrument drift.

Table 3.3 summarizes the TriOS Ramses-ACC specifications. Both radiometers are applied in Chengdu, Beijing, Lhasa and Shegatse for a specific time period. Specific information can be found in Table 3.4.

Table 3.3: TriOS Ramses-ACC performance specifications.

Radiometers	RAMSES-ACC-VIS	RAMSES-ACC-UV
Wavelength range	320 - 950 (nm)	280 - 500 (nm)
Spectral sampling	3.3 nm/pixel	2.2 nm/pixel
Spectral accuracy	0.3 nm	0.2 nm
Usable channels	190	100
Accuracy	better than 6 - 10%	better than 6 - 10%
Operatingtemperature	-10 $°C$ to +50 $°C$	-10 $°C$ to +50 $°C$

Table 3.4: TriOS Ramses-ACC measurement site information

Site	Latitude [°N]	Longitude [°E]	Altitude [m]	Measured time period and date
Chengdu	30.68	104.06	500	12:30:00 to 12:45:00 (06/07/2015)
Beijing	39.93	116.42	50	12:49:00 to 12:59:00 (08/07/2015)
Lhasa	29.65	91.18	3683	14:00:00 - 14:15:00 (21/07/2015)
Shegatse	29.25	88.88	3837	14:10:00 -14:25:00 (11/07/2015)

On 8th of July 2015, Beijing was moderately polluted, according to measured results by Beijing Environmental Protection Monitoring Centre and U.S Embassy Beijing Air Quality Monitor. The air condition of Beijing on that day is shown in Figure 3.10.

Figure 3.10: TriOS Ramses-ACC-VIS and Ramses-ACC-UV in Beijing, 08/07/2015.

The weather condition in Chengdu is shown in Figure 3.11. On 6th of July 2015, Chengdu had a relatively good weather. TriOS Ramses-ACC-VIS and Ramses-ACC-UV are not visible in this figure. They were mounted on the top of the building to the left.

Figure 3.11: Chengdu weather on 06/07/2015, TriOS Ramses-ACC-VIS and Ramses-ACC-UV were mounted on the top of the left building.

Chapter 4

Analysis and results

This chapter presents the results which answer each of our research questions. It is divided into four parts.

In subsection 4.1, the temporal and spatial variation of the solar irradiance in Tibet and the daily radiant exposure are presented. In subsection 4.2, the Yearly averaged Aerosol Modification Factor (YAMF) and the atmospheric transmittance in Tibet are compared with those in mainland China. In subsection 4.3, the Yearly averaged Cloud Modification Factor (YCMF) is calculated and also the maximum available annual solar energy. Finally, a sensitivity study is presented in subsection 4.4.

4.1 Solar irradiance measurements

The solar irradiance measurements and their temporal and spatial variations are analyzed hereinafter for Lhasa, Nagchu, Tingri, and Nyingchi from July 2010 to December 2012. The analysis includes the solar irradiance, the daily radiant exposure, and the monthly average of the daily radiant exposure. Moreover, the yearly radiant exposure is calculated in order to estimate the YCMF, i.e. the cloud conditions in Tibet.

4.1.1 Solar irradiance measurements

Solar irradiance measurements were conducted in Lhasa (July 2010 - Sept 2012), Nagchu (July 2010 - Nov 2013), Tingri (2010, 2012), and Nyingchi (2010). The solar irradiances averaged over all available measurements at the four sites during 2010, 2011, 2012, and 2013 are illustrated in Figure 4.1. The redder the pixels, the stronger the irradiance values. At around 06:00 Universal Time Coordinated (UTC) (local noon), the highest irradiance values are observed.

In Figure 4.1, the cloud free days are more frequent in the wintertime. For Lhasa (a), high irradiance values were measured more frequently during April to June compared to the rest of the year. However, the high irradiance values in Nagchu (b) are more symmetrically distributed with respect to the middle of the year (around 15th of June), because the rain is almost evenly distributed throughout the year. Tingri (c) has the best solar energy potential based on available data. A distinct rainy season is observed from mid June to end of September. Despite of the short rainy season, Tingri has more sunshine hours and has little disturbance of clouds for the rest of the year. In Nyingchi (d), the irradiance is considerably lower from mid August to mid October, and seldomly the irradiance values

exceed 1000 W m^{-2}.

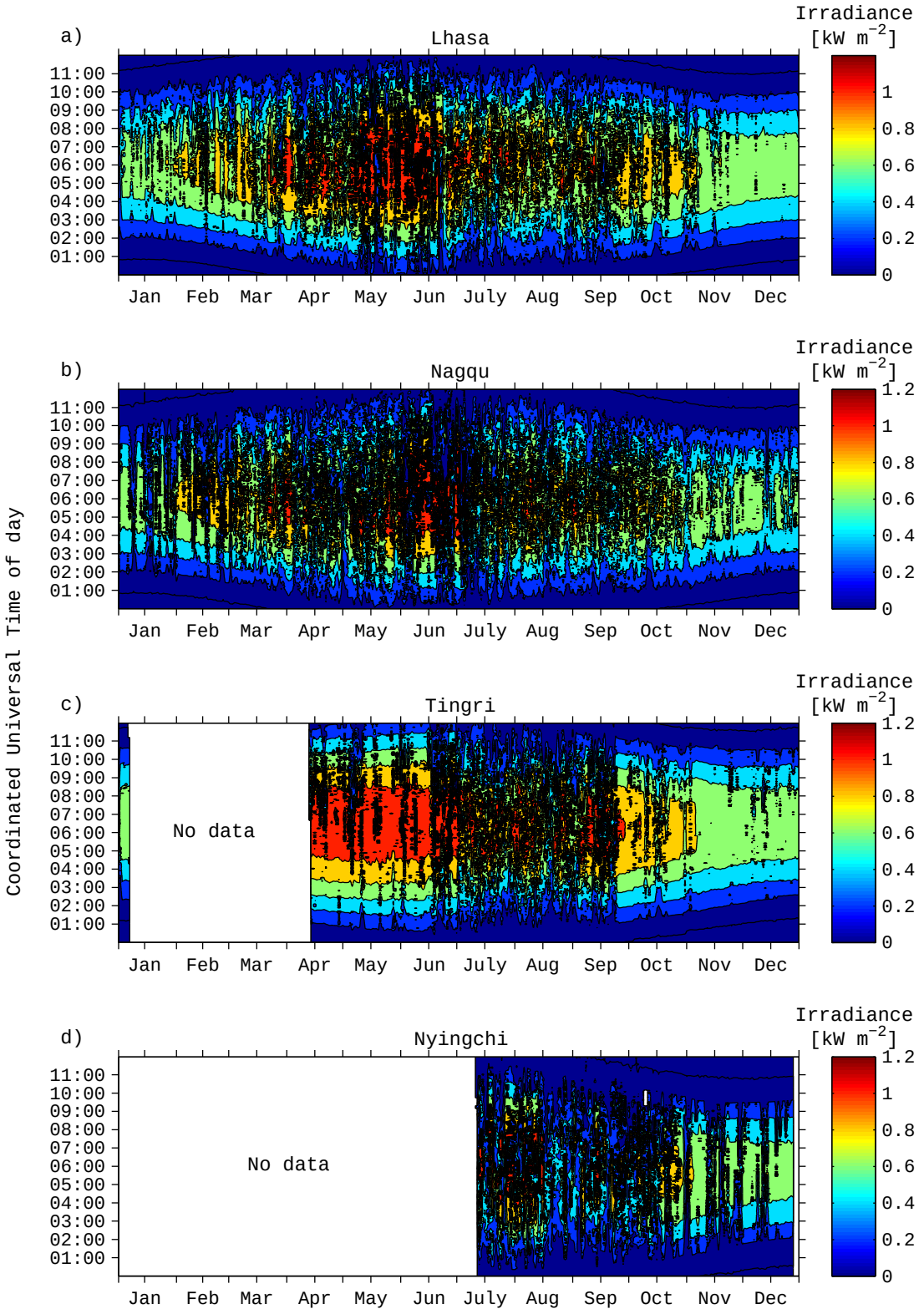

Figure 4.1: Averaged solar irradiance over all measured years for Lhasa (a), Nagchu (b), Tingri (c) and Nyingchi (d). Time on the vertical axis is given as UTC, where local noon is about 06:00 UTC.

Generally speaking, high irradiance levels (around 1200 W m^{-2}) are observed at noon in summer, and irradiance levels around 720 W m^{-2} are observed at noon in winter at all four sites. In Lhasa and Nagchu, there are about 25 and 26 hours in a year having irradiance values from 1200 to 1300 W m^{-2} (Figure 4.2). In comparison, from the modeled TOA irradiance values (see subsection 4.3) for Lhasa and Nagchu, there are about 467 hours (Lhasa) and 415 hours (Nagchu) in a year having irradiance values from 1200 to 1300 W m^{-2} (Figure 4.14).

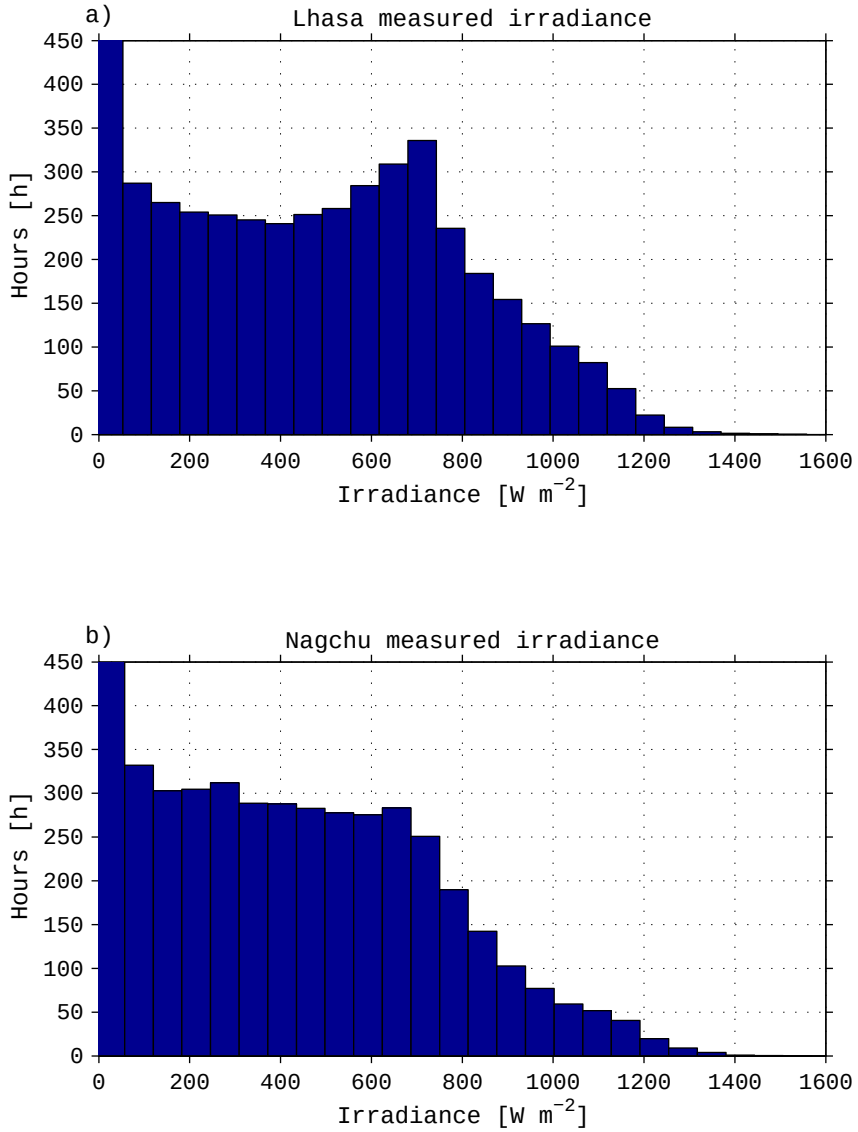

Figure 4.2: Measured irradiance levels and corresponding sun shine hours in one year in Lhasa (a) and Nagchu (b). The first bins in (a) and (b) are cut to view the histogram better. The cut values are 4807 hours in (a) and 4865 hours in (b), these long time periods are caused by night time measurements.

The maximum value observed in Lhasa and Nagchu in a year can reach up to 1558 W m^{-2} and 1569 W m^{-2}, whereas the maximum irradiance at TOA is only about 1300 W m^{-2} (accounting for the solar zenith angle cosine factor). These measured extreme irra-

diance values exceeding 1300 W m^{-2} last about 6 to 7 hours at both sites in a year. This phenomenon can be explained by the enhancement effect of broken bright clouds on a clear sky. When several clouds are surrounding the sun, but not blocking it, the diffuse radiation increases as a result of strong scattering (Antón et al., 2012).

The irradiance values at TOA are modeled assuming yearly average sun-earth distance. But in the summer of northern hemisphere the Sun-Earth distance is 3% longer compared to that in the summer of the southern hemisphere due to the elliptical orbit of the Earth. Therefore, the summer irradiance is 6% lower in the northern hemisphere than the summer irradiance in the southern hemisphere. By assuming an average sun-earth distance, the maximum summer TOA irradiance discussed here is about 3% higher than the real irradiance. But since the instrument has 5% uncertainty, this seasonal variation has been neglected.

Table 4.1: Observed yearly radiant exposures.

	Lhasa	Nagchu	Tingri	Nyingchi
Altitude [m]	3683	4510	4335	2995
Latitude [°N]	29.65	31.47	28.66	29.66
Observation (whole year) [GJ m^{-2}]	7.6	6.8	Lack of data	Lack of data
Observation (14th Apr to 31st Dec) [GJ m^{-2}]	5.7	5.0	6.0	Lack of data
Observation (12th July to 28st Dec) [GJ m^{-2}]	3.3	3.1	3.4	2.7

In Table 4.1, the yearly radiant exposures of Lhasa and Nagchu are obtained using the average of all available measurements in 2010, 2011, 2012 and 2013. Every year, about 7.6 GJ energy can be obtained from one square meter horizontal surface in the capital city of Tibet. The amount of the annual energy in Nagchu is about 10% less than in Lhasa, i.e. 6.8 GJ m^{-2}. Based on the valid observation period from mid April to end of December, Tingri has the highest radiant exposure (about 5% higher than Lhasa and 20% higher than Nagchu). The radiant exposure calculated from mid July to end of December indicates that Nyingchi has a relatively low value compared to the rest of sites (about 21% lower than Tingri, 13% lower than Nagchu and 18% lower than Lhasa). The cause of this difference is due to altitude, latitude and weather effects (discussed in subsection 4.3.1). The total power consumption in the prefecture of Lhasa in 2014 was about 6.5 petajoules ($6.5 \cdot 10^{15}$J) (personal communication: State Grid Corporation of China). In order to cover the yearly power consumption in the Lhasa prefecture, 0.85 km^2 and 0.95 km^2 of solar panels are needed to receive sunlight for a year, assuming a yearly radiant exposure of 7.6 and 6.8 GJ m^{-2} and a 100% light-electricity transformation efficiency. For typical light-electricity transformation efficiency of 16%, about 5.3 km^2 and about 5.9 km^2 of solar panels are required for the same yearly radiant exposures.

Figure 4.3 shows the seasonal variation of daily radiant exposure (daily integrated solar irradiance) at all four sites from 2010 - 2013. In this figure, the curves for Lhasa and Nagchu are very similar. Between July 2010 and July 2012, the daily radiant exposure reaches values up to about 33 MJ m^{-2} for clear summer days and down to 15 MJ m^{-2}

for clear winter days. The low daily radiant exposure in a winter clear day is only about 54 % compared to a clear mid summer day. In winter 2013, a very low value about 13 MJ m^{-2} was observed on a clear day in Nagchu. The daily radiant exposure in Tingri is slightly higher than that of Lhasa and Nagchu, due to a different geographical location (low latitude and high altitude, see in Table 4.1). In contrast, the values for Nyingchi are slightly lower than for the other sites, due to a more humid and cloudy climate, and lower altitude. The maximum daily radiant exposure for clear summer days is around 29 MJ m^{-2} and the minimum value is around 14 MJ m^{-2} for clear winter days in Nyingchi.

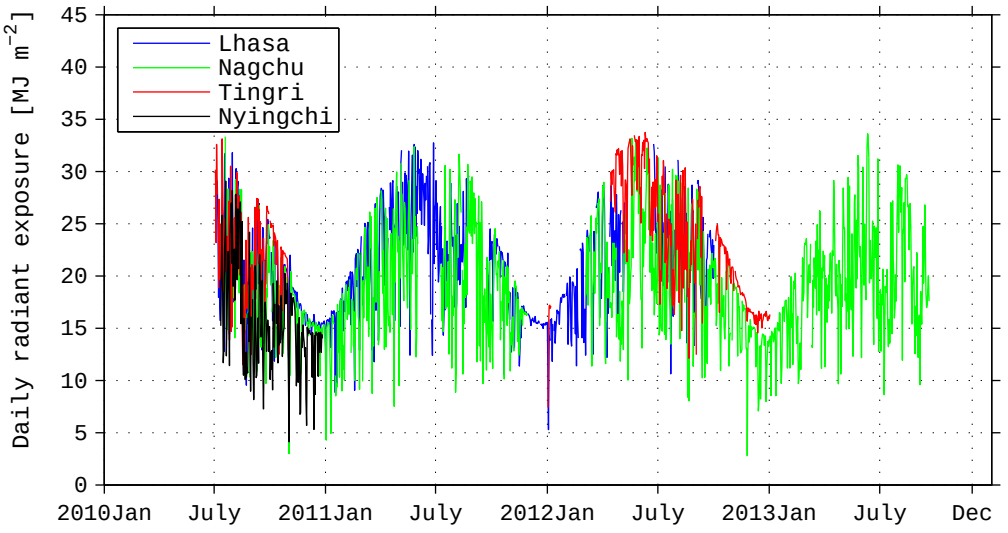

Figure 4.3: Daily radiant exposure at four sites in Tibet (2010 - 2013).

In order to learn more about the distinction of daily radiant exposure, the monthly averaged daily radiant exposures are shown in Figure 4.4.

By averaging out the extreme values, the average provides a more general and more reliable daily radiant exposure value. Figure 4.4 distinctly illustrates that Tingri has the highest daily radiant exposure among the four sites, while Nyingchi has the lowest. Lhasa has a richer solar energy resource than Nagchu.

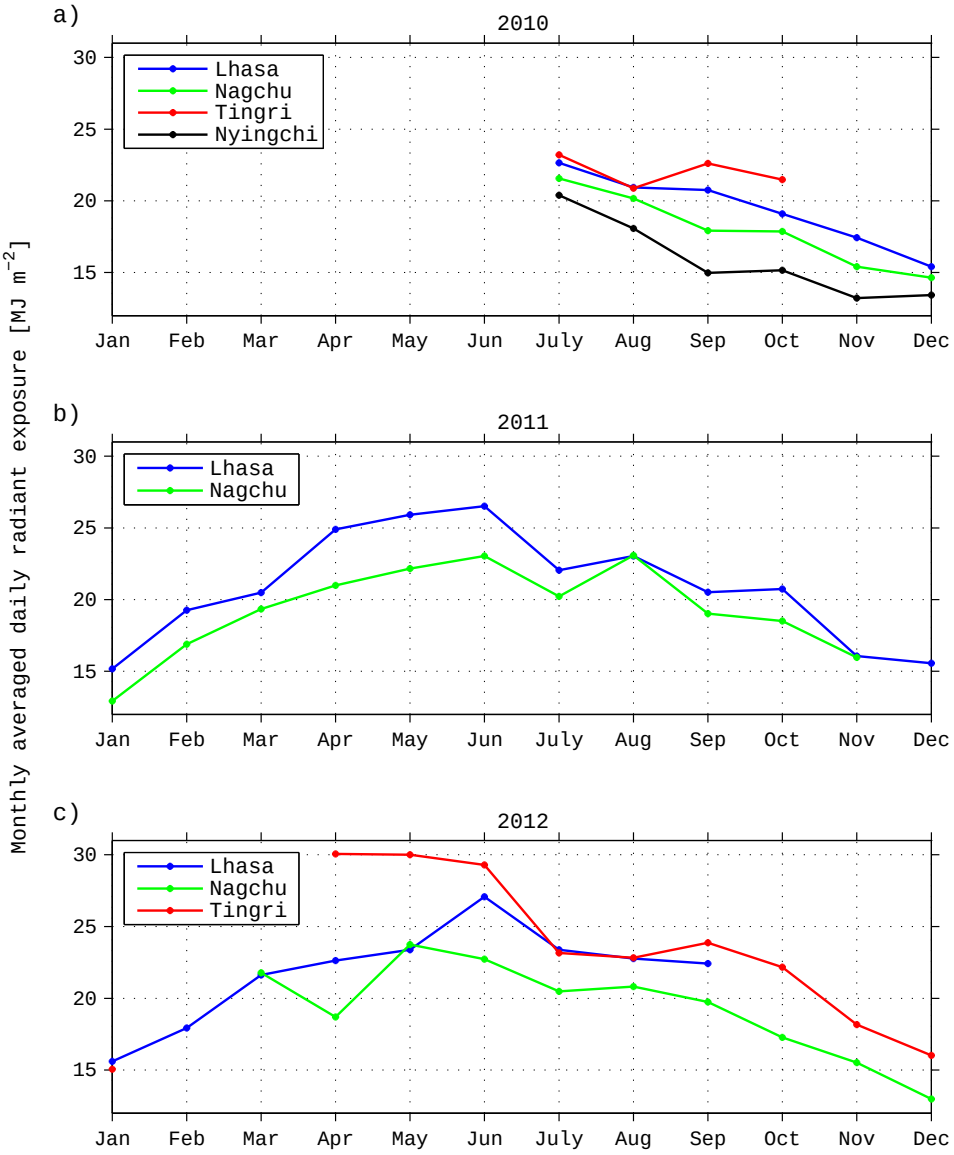

Figure 4.4: Monthly averaged daily radiant exposures in 2010 (a), 2011 (b), and 2012 (c) for Lhasa, Nagchu, Tingri, and Nyingchi.

To quantify this difference, the yearly averaged value for daily radiant exposures can be conveniently calculated by taking the mean value of monthly averaged daily radiant exposures. Therefore, the solar energy resources at these four sites can be formally compared. Taking all available years into account, the yearly averaged daily radiant exposures are 21 MJ m^{-2}, 19 MJ m^{-2}, 23 MJ m^{-2} and 16 MJ m^{-2} for Lhasa, Nagchu, Tingri, and Nyingchi, respectively (averaged from 2010 to 2013). In comparison, a five year averaged daily radiant exposure was about 21 MJ m^{-2} in Gaize (northwestern Tibet) from 2001, calculated by Liu et al. (2012). This value shows a good consistency with our results.

4.2 Yearly averaged aerosol modification factor (YAMF)

To estimate the air quality for the sites in Tibet in comparison to other sites in China, the YAMF (the effect of aerosols on the yearly received solar energy) is calculated in this subsection under cloudless condition. The YAMF is defined as the ratio of the yearly radiant exposure measured for a certain aerosol optical depth to the yearly radiant exposure under clear sky conditions. Firstly, the Aerosol Optical Depths (AODs) for our four sites need to be determined. Hereby, AccuRT is used to fit the measured spectra in Chengdu, Bejing, Lhasa, and Shegatse. So, the AODs in these places can be determined as well as the transmittance of the atmosphere at our four sites using the modeled TOA spectral irradiances. Secondly, the irradiance of a whole year is modeled by applying the obtained AODs. Finally, the yearly radiant exposures with certain AODs and the yearly radiant exposure under clear sky conditions are calculated to decide the YAMFs for the four sites.

4.2.1 Quality estimation of AccuRT

The required quality of the irradiance simulated by AccuRT needs to be determined before the modeling can be performed. The inaccuracy of the pyranometer is 5%, thus, the modeled irradiances do not need to have a higher accuracy than 5%.

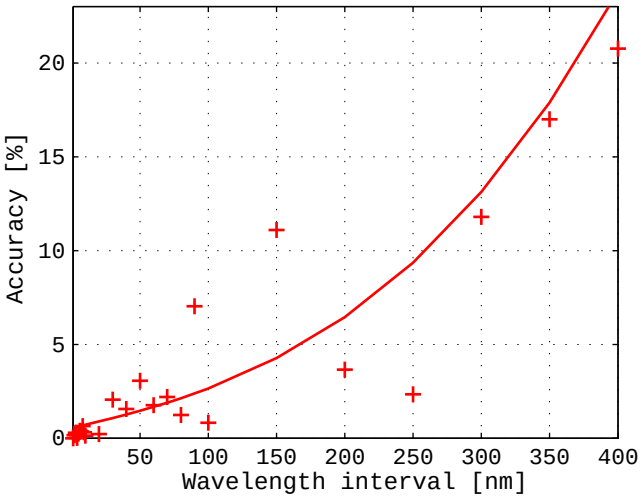

Figure 4.5: Wavelength interval dependent accuracy of the irradiance calculated by AccuRT at 0° solar zenith angle.

Figure 4.5 illustrates the fitted curve for the accuracies of AccuRT calculated irradiance at a 0° solar zenith angle by following equation:

$$Accuracy\ [\%] = 100 \times (E_{\Delta\lambda} - E_{1nm})/E_{1nm}\ [\%] \tag{4.1}$$

E_{1nm} is the irradiance integrated over the whole spectrum, where 1 nm represents the sampling wavelength resolution. $E_{\Delta\lambda}$ is the integrated irradiance over the whole spectrum using $\Delta\lambda$ as the sampling wavelength resolution. It can be seen that a wavelength interval of roughly 180 nm is necessary to keep the inaccuracy below 5%. In this study,

the wavelength interval of 50 nm is chosen to assure that the accuracy is well below 5%. Thus, the wavelength interval of 50 nm is used to fit measured irradiances with the modeled irradiances.

As an example, Figure 4.6 illustrates comparisons between modeled (red line) and measured (green line) irradiances for Lhasa, Nagchu, Tingri, and Nyingchi on a sunny day. It can be seen that the maximum irradiance reached up to 889 W m^{-2} (Lhasa), 891 W m^{-2} (Nagchu) and 899 W m^{-2} (Tingri) at noon on 25th October 2010. To avoid rainy weather, 9th of November (sunny) 2010 was chosen for Nyingchi and 755 W m^{-2} was observed at midday.

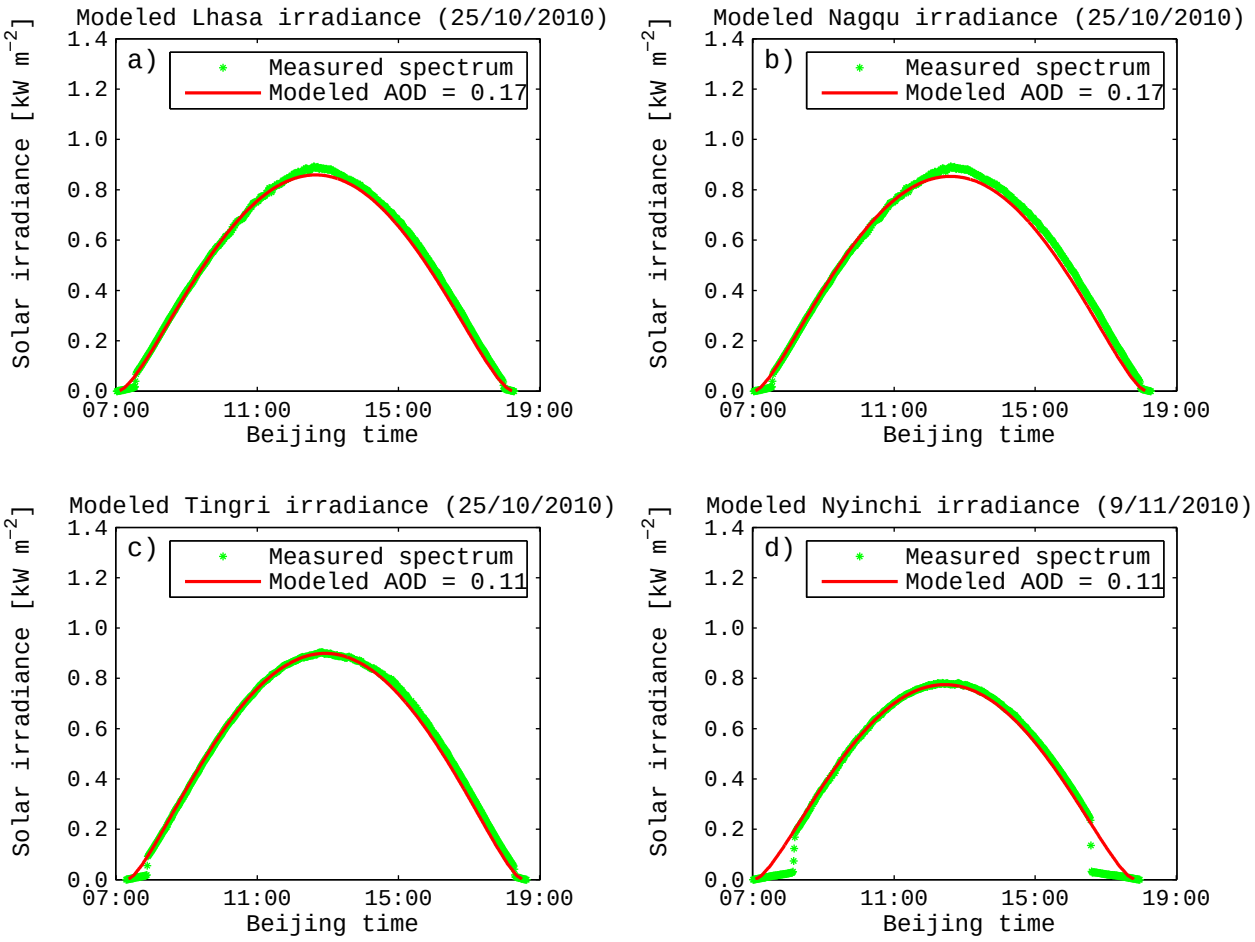

Figure 4.6: Modeled and observed solar irradiances in Lhasa (a), Nagchu (b), Tingri (c), Nyingchi (d) for one day in 2010. AOD is given at 580 nm.

According to Xia et al. (2008), typical AOD values vary from 0.11 to 0.27 at 580 nm from winter to spring on the Tibetan Plateau. In this modeling process on an autumn day, an AOD of 0.17 was chosen for Lhasa and Nagchu to get the best fit, whereas an AOD of 0.11 was applied for Tingri and Nyingchi. The amount of applied water vapour in the model was neglectable at this time of the year and all local altitudes were used in the AccuRT simulations.

The modeled and measured irradiance curves show very good agreement, although, the measured irradiance curves are a little bit asymmetric compared to the modeled irradiance

curves for all cases. This asymmetry is less than the instrument inaccuracy, therefore, a reliable result of yearly modeled irraidiances can be estimated by AccuRT.

4.2.2 Solar spectrum measurements

RAMSES-ACC-VIS and RAMSES-ACC-UV (from TriOS) are used to measure the downward spectral irradiance. The spectral irradiance value is measured every minute during a certain time period in July (Figure 4.7).

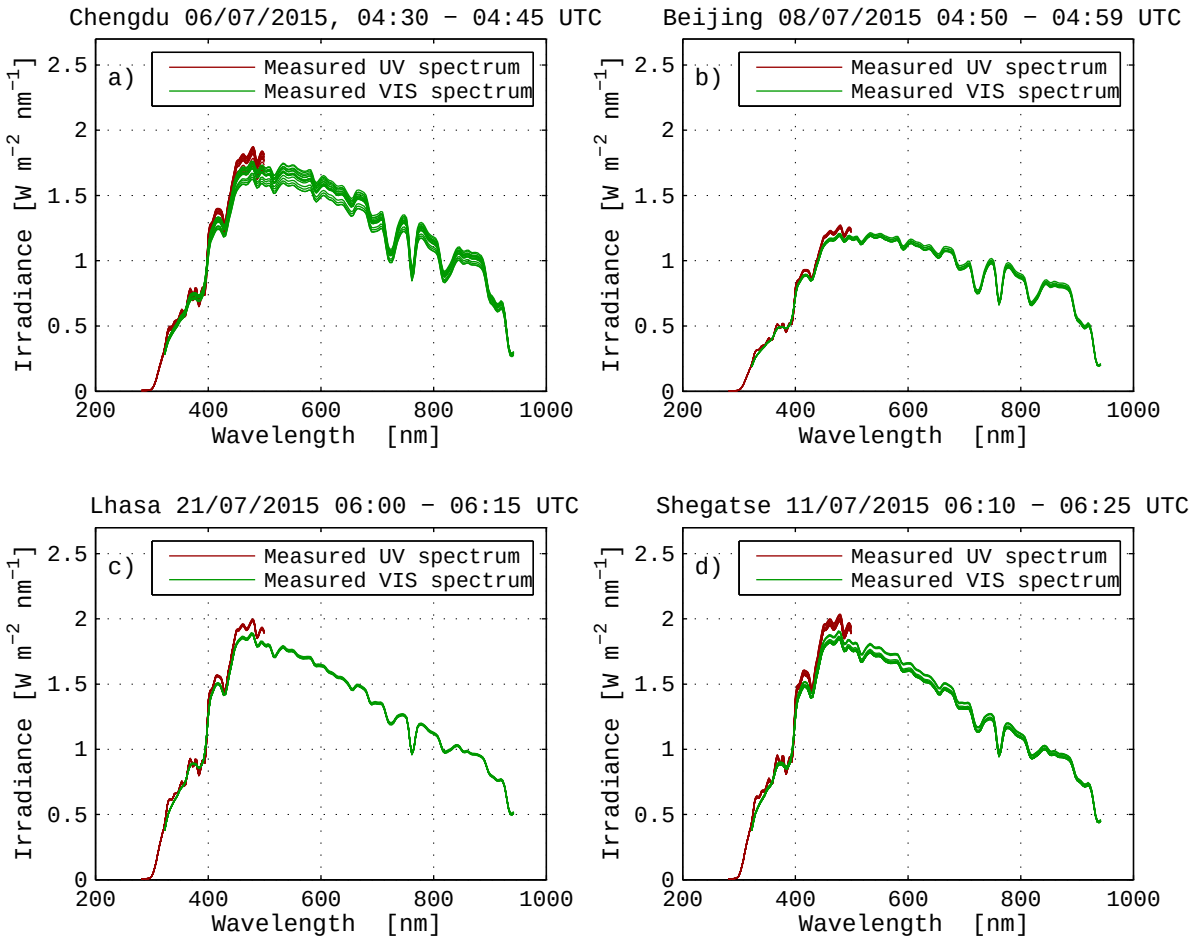

Figure 4.7: Measured spectra in Chengdu, Beijing, Lhasa, and Shegatse.

In Figure 4.7, the disagreement between the spectra measured by RAMSES-ACC-UV (red line) and by RAMSES-ACC-VIS (green line) might be caused by calibration inaccuracy of the instruments and possibly alignment errors of the two radiometers. For Chengdu (a), the measured spectra are probably affected by a thin cloud layer. However, in Lhasa (c), the spectra are almost identical, having no cloud influence during 15 min around 06:00 UTC. On the 8th of July the Beijing air quality level was ranked as moderately polluted, according to China's Ministry of Environmental Protection (MEP). This can also be seen in the Beijing (b) spectra, which are significantly lower than the spectra from the other sites.

In order to obtain knowledge of the atmospheric differences between Chengdu, Beijing, Lhasa, and Shegatse, the transmittances for the four sites are plotted in subsection 4.2.4.

4.2.3 AODs in four sites

AccuRT was applied to model spectral irradiances in Chengdu, Beijing, Lhasa and Shegatse. The modeled spectral irradiances and the measurements have to agree with each other. During the fitting process, several atmospheric parameters are varied, to obtain the best fit (see Table 4.2).

Table 4.2: Particle radii, volume fractions and scaling factors for atmospheric component in Chengdu, Beijing, Lhasa and Shegatse.

	Chengdu	Beijing	Lhasa	Shegatse
Partical radii fine mode [μm]	0.13	0.023	0.13	0.13
Partical radii coarse mode [μm]	2.5	2.5	2.5	2.5
Aerosol volume fraction	$3.5{\cdot}10^{-11}$	$8.1{\cdot}10^{-10}$	$1.0{\cdot}10^{-11}$	$1.5{\cdot}10^{-11}$
Fine mode fraction	0.9	0.8	0.99	0.99
Water vapour column	2.8	2.8	0.50	0.66
Molecular scattering	1.0	1.0	0.64	0.62
Ozone column	1.0	1.0	1.0	1.0

As can be seen in Table 4.3, an AOD of 0.29, 0.47, 0.09 and 0.13 at 580 nm are found in Chengdu, Beijing, Lhasa and Shegatse, respectively. The AOD of Chengdu could also be influenced by thin clouds. The best fit modeled by AccuRT is denoted as the black curves in Figure 4.8. This fitted spectra is obtained after applying Gaussian smoothing to the modeled spectral irradiance (sampled every 1 nm), using a bandwidth of 4.5 nm.

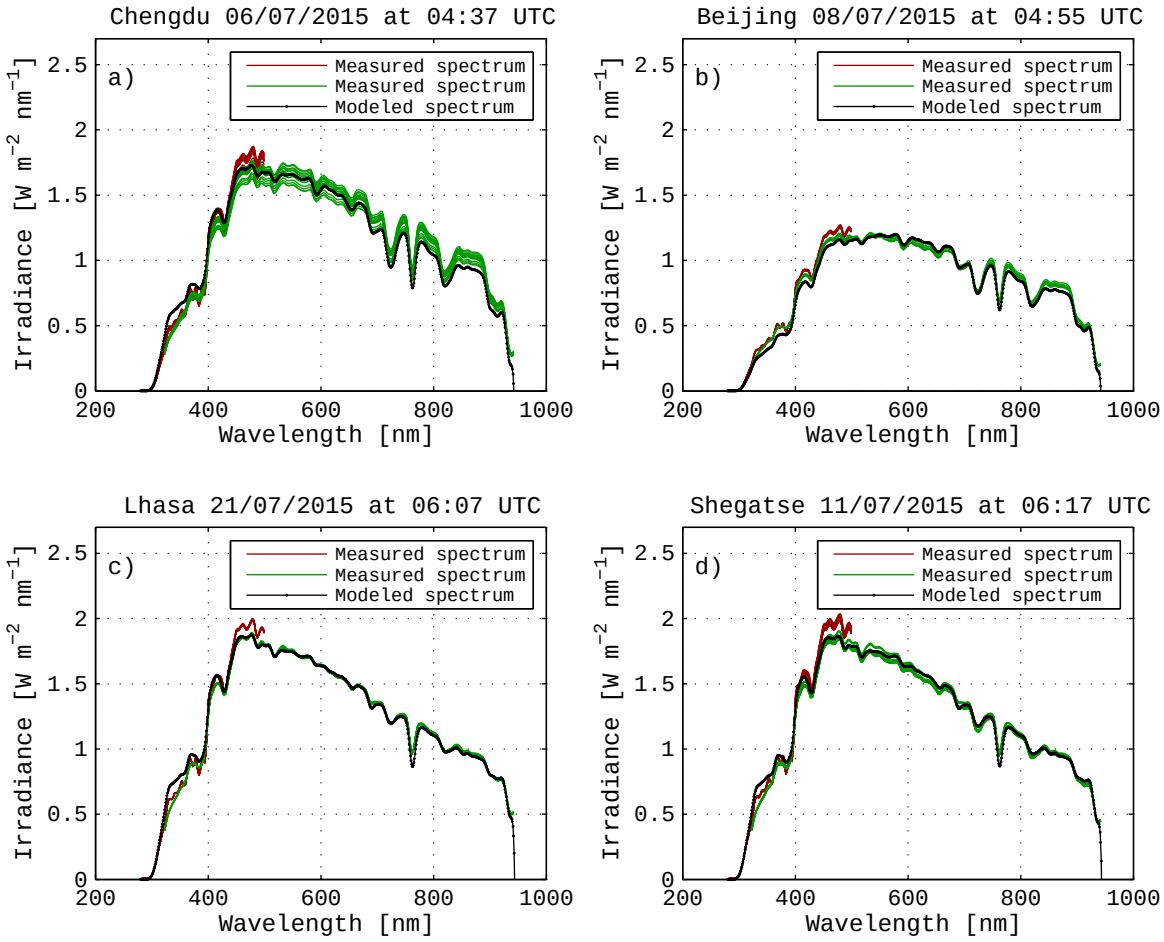

Figure 4.8: Measured and modeled spectra in Chengdu, Beijing, Lhasa, and Shegatse.

4.2.4 Aerosol disturbed yearly radiant exposure

Yearly radiant exposures for cloudless days are calculated based on the obtained AOD from subsection 4.2.3, in Chengdu, Beijing, Lhasa and Shegatse, respectively. The no cloud and no aerosol yearly radiant exposures are also calculated in order to compute the YAMF.

Table 4.3: Yearly radiant exposure under modeled AOD and YAMF.

	Chengdu	Beijing	Lhasa	Shegatse
AOD (at 580 nm)	0.29	0.47	0.09	0.13
Clear day [GJ m^{-2}]	8.0	7.1	8.9	8.9
Cloudless day [GJ m^{-2}]	7.3	4.6	8.6	8.6
YAMF	0.92	0.64	0.97	0.96

Beijing has the highest AOD, and the sunlight intensity of a whole year will be reduced by 36% by this high AOD value. In contrast, Chengdu, Lhasa, and Shegatse have much less aerosols on a cloudless day. To obtain some information about the atmospheric compositions in Chengdu, Bejing, Lhasa, and Shegatse, the spectra at the TOA are modeled to compute the transmittance. Transmittances are calculated as the ratio of the modeled

spectra at surface to the modeled spectra on the TOA. The spectral transmittances of

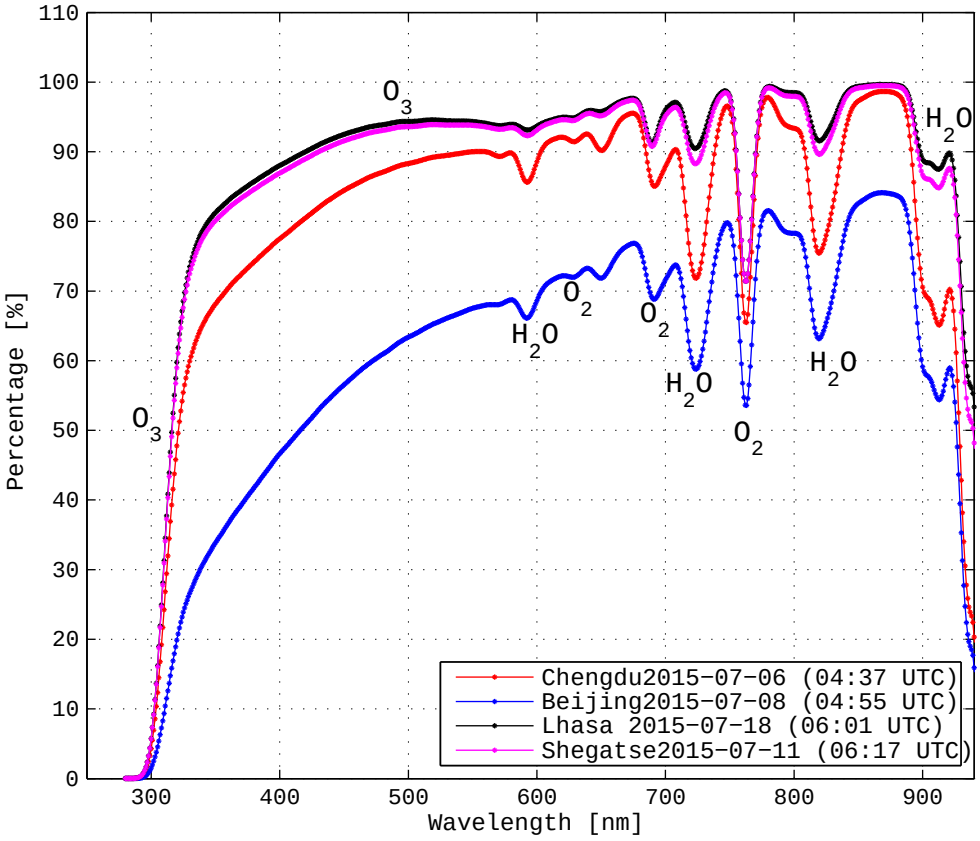

Figure 4.9: Atmospheric transmittance in Chengdu, Beijing, Lhasa, and Shegatse. The absorption bands of different gases are marked in the figure.

the atmosphere in Chengdu, Beijing, Lhasa and Shegatse are displayed in Figure 4.9. In addition to aerosols, the most important substances that reduce sunlight in the spectrum from 300 nm to 950 nm are O_3, O_2, and H_2O. The wavelength regions where the spectral irradiance is absorbed by O_3, O_2, and H_2O molecules are shown in Fig 4.9. Rayleigh scattering is responsible for the attenuation in the short wavelength range. In Figure 4.9, Lhasa and Shegatse have the most transparent atmosphere and Lhasa has less water vapour absorption at 06:01 UTC on 18th July 2015. The transmittance for Beijing is considerably lower due to the high AOD, and the water vapour in Beijing and Chengdu is considerably higher than in Lhasa and Shegatse.

4.3 Yearly averaged cloud modification factor (YCMF)

In order to get details about the weather situation in Lhasa and Nagchu, the YCMF is calculated for these two sites with the help of AccuRT. As mentioned earlier, the YCMF is the ratio of the calculated yearly radiant exposure to the modeled yearly radiant exposure under clear sky conditions (no clouds and no aerosols). AccuRT is therefore used to model the yearly radiant exposure under clear sky condition.

4.3.1 Yearly modeled irradiances

Under clear sky (no cloud no aerosol) condition, the maximum possible yearly radiant exposures in Lhasa, Nagchu, Tingri, Nyingchi both for the real altitudes and for corresponding locations at sea level are listed in Table 4.4. Moreover, to investigate the latitude and altitude dependence of the yearly radiant exposure, the four observation sites are first modeled having the same height as Lhasa and later the same latitude as Lhasa. The corresponding yearly radiant exposure values are also tabulated in Table 4.4.

Table 4.4: Yearly radiant exposure in various circumstances.

	Lhasa	Nagchu	Tingri	Nyingchi
Altitude [m]	3683	4510	4335	2995
Latitude [° N]	29.65	31.47	28.66	29.66
Observation (whole year) [GJ m^{-2}]	7.6	6.8	Lack of data	Lack of data
Clear day [GJ m^{-2}]	8.9	8.8	9.0	8.8
Sea level clear day [GJ m^{-2}]	8.4	8.3	8.5	8.4
Lhasa height (3683m) [GJ m^{-2}]	8.9	8.7	8.9	8.9
Lhasa latitude (29.65° N) [GJ m^{-2}]	8.9	9.0	8.9	8.8
YCMF	0.85	0.77	Lack of data	Lack of data

From Table 4.4, Tingri has the highest modeled yearly radiant exposure of about 9 GJ m^{-2}, due to the high altitude in combination with low latitude. For Nagchu, although it has the highest altitude, the maximum possible yearly radiant exposure is slightly lower due to its northernmost location.

To study the altitude effect, the irradiance values on the sea level are investigated. AccuRT is applied by keeping longitude and latitude fixed. The modeled yearly radiant exposure at sea level is 5% lower than at the altitude of Lhasa (3683 m), 6% lower than that of Nagchu (4510 m), 5% lower than that of Tingri (4335 m) and 4% lower than that of Nyingchi (2995 m). Thus, places at sea level, but at the same latitude do have lower annual solar energy. The corresponding modeled clear day irradiances (no cloud no aerosol) on the sea level throughout a year are displayed in Figure 4.10.

Furthermore, the cloud effect is studied. Under no cloud and no aerosol condition, the yearly amount of energy increases from 7.6 GJ to 8.9 GJ per unit surface in Lhasa and from 6.8 GJ to 8.8 GJ in Nagchu. Based on the YCMF, 15% of the yearly radiant exposure is affected by aerosols and cloudy or rainy weather in Lhasa and about 23% in Nagchu. Therefore, Nagchu is influenced by clouds and aerosols more frequently through out a year. The corresponding modeled irradiances for clear days (no cloud no aerosol) throughout a year is shown in Figure 4.11. In comparison, the modeled irradiances for

Bergen (60 °N, Norway) and Sahara desert for clear days are also shown in Figure 4.12 and Figure 4.13 throughout a year. The site Matam, Senegal in the Sahara desert is chosen due to a relatively low latitude, which is about 15.6 °N. The yearly radiant exposure is about 5.1 GJ m^{-2} for Bergen and 9.4 GJ m^{-2} for Matam. In terms of yearly energy, a cloud free Bergen would receive almost half of the energy compared to Matam. However, Bergen has a higher daily radiant exposure (30 MJ m^{-2}) compare to Matam (29 MJ m^{-2}) in the summer time. This phenomenon is caused by the high number of sunshine hours in Bergen during summer time (no rain assumed).

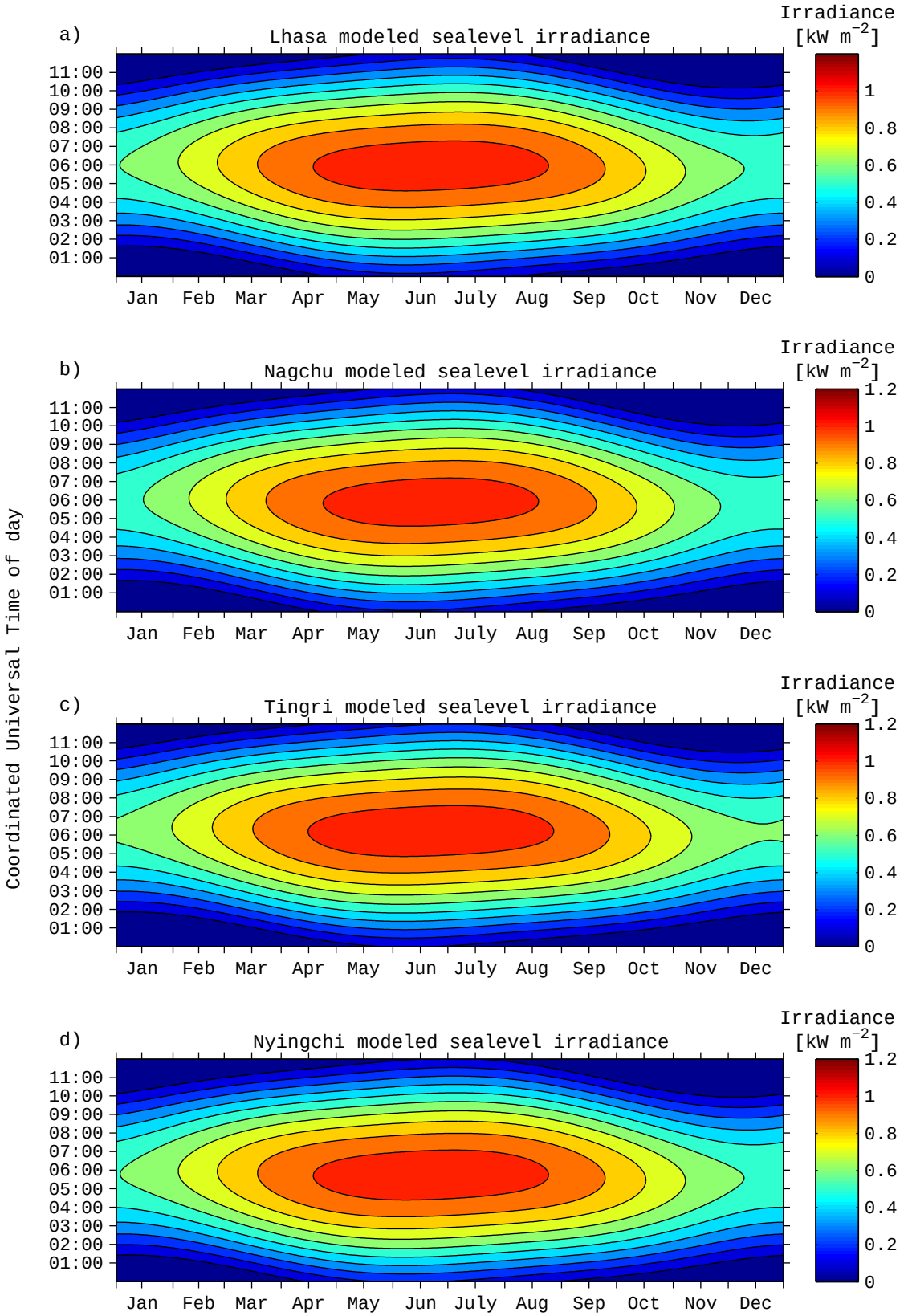

Figure 4.10: Modeled irradiance on sea level for Lhasa (a), Nagchu (b), Tingri (c), and Nyingchi (d).

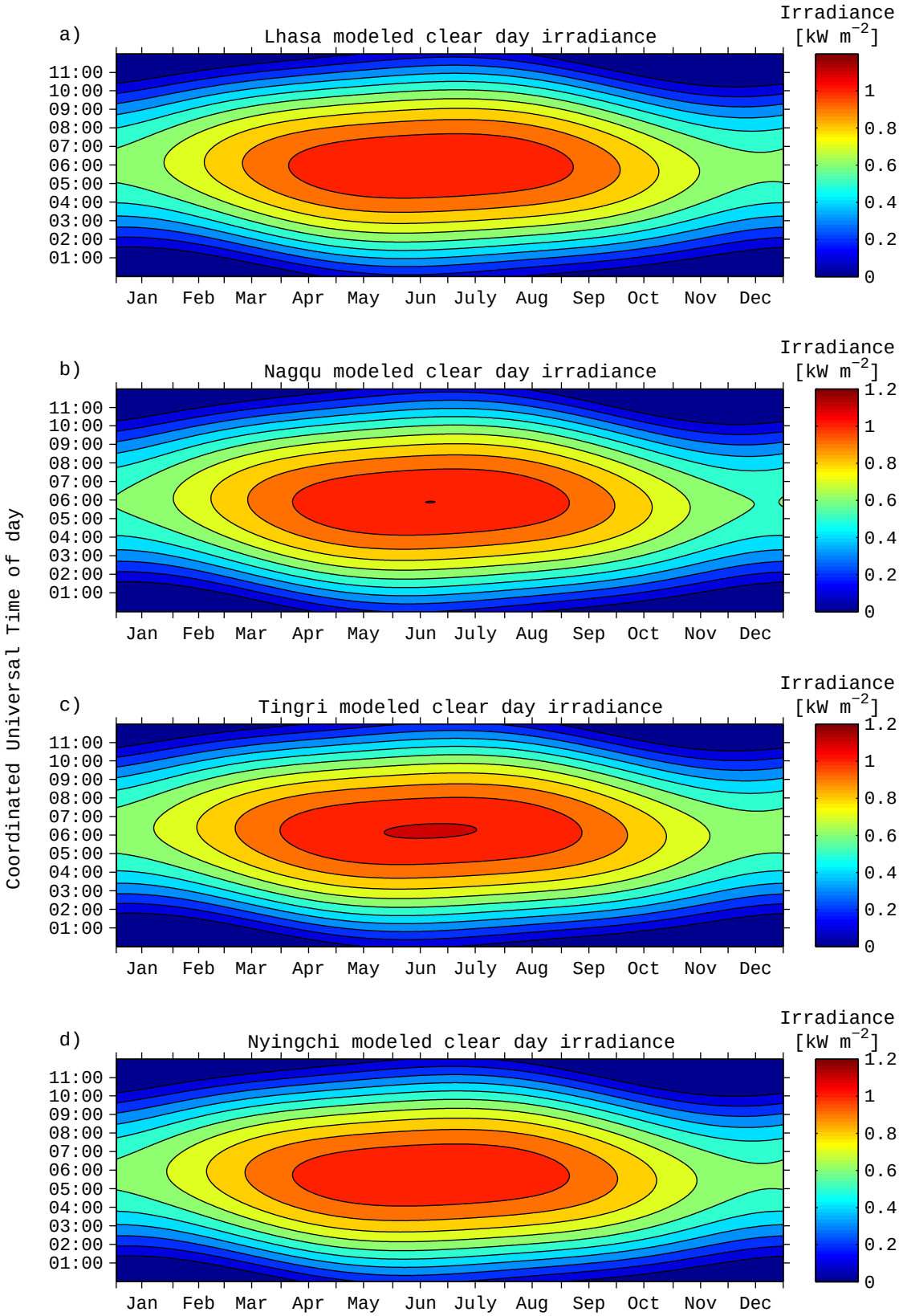

Figure 4.11: Modeled clear day irradiance for Lhasa (a), Nagchu (b), Tingri (c), and Nyingchi (d).

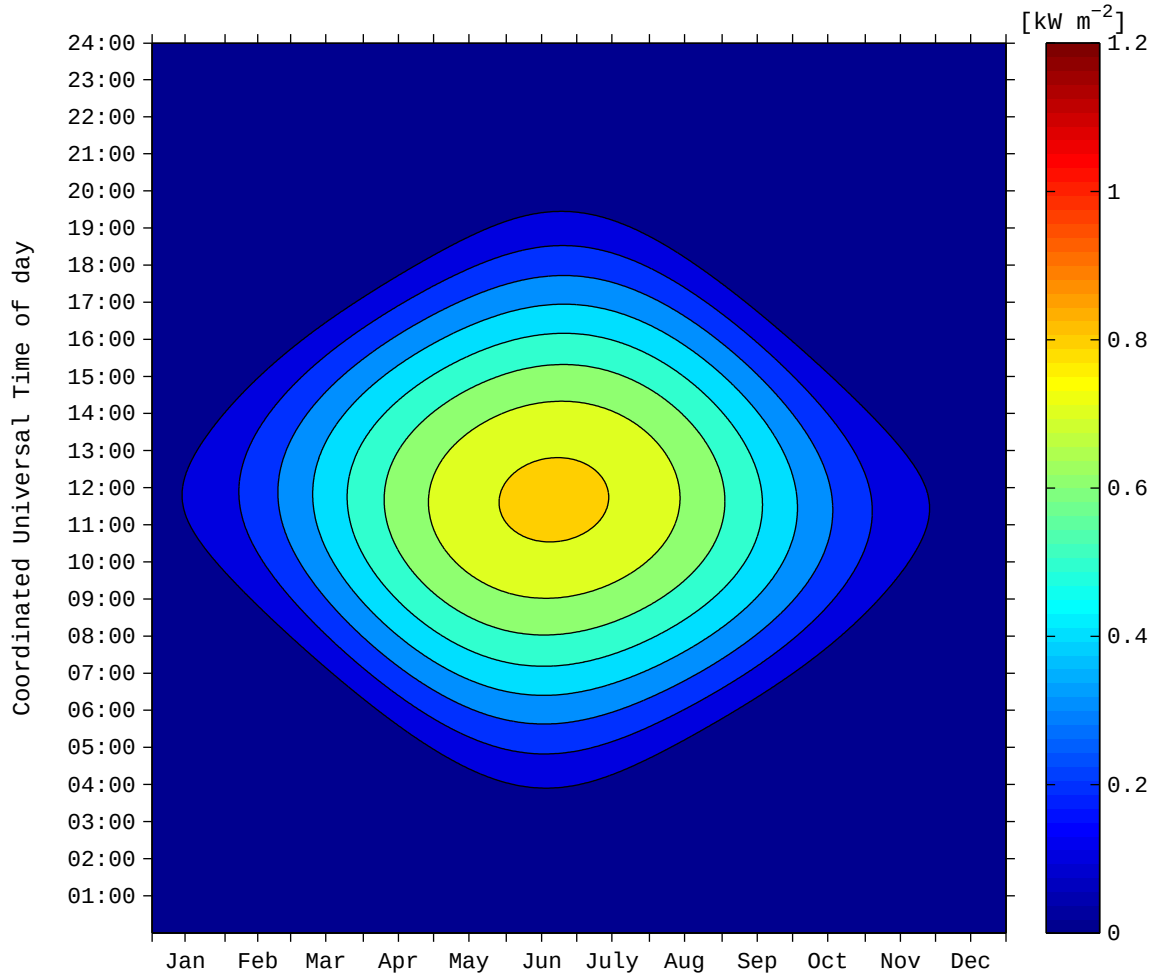

Figure 4.12: Modeled clear day irradiance in Bergen.

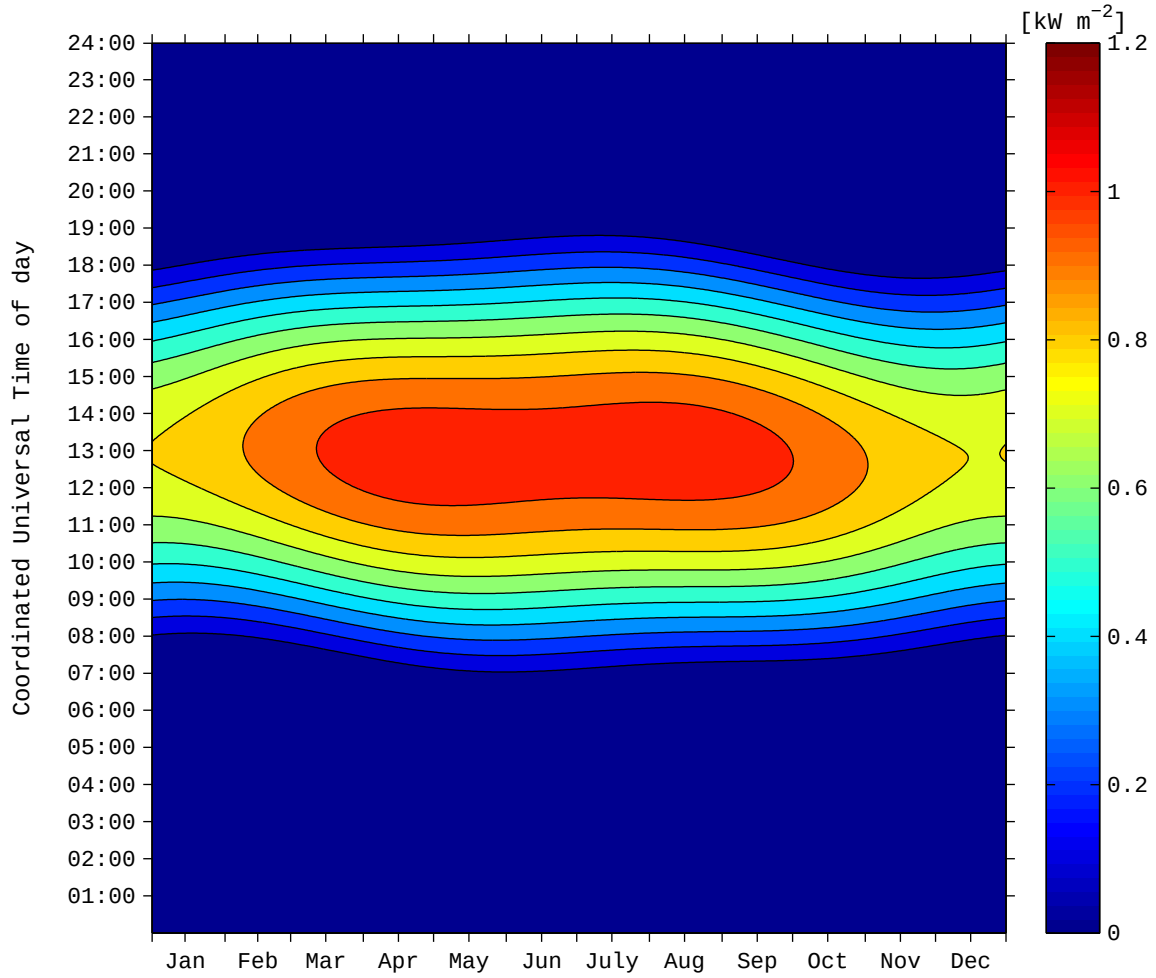

Figure 4.13: Modeled clear day irradiance in Matam, Senegal in the Sahara desert.

On the one hand, yearly radiant exposure ranges from 8.7 GJ m^{-2} to 8.9 GJ m^{-2} (Table 4.4) due to a latitude difference of 2.8 degree if all sites are considered to be at the same height. On the other hand, the yearly radiant exposure ranges from 8.8 GJ m^{-2} to 9.0 GJ m^{-2} due to an altitude difference of 1515 m if all the sites are considered to be at the same latitude. In short, a variation of 2.8 degree in latitude causes a change of 2% and a variation of 1515 m in altitude also causes a change of 2% in the yearly radiant exposure.

Therefore, the yearly radiant exposure is influenced equally by latitude and altitude at the four sites in Tibet, whereas the weather (YCMF) has a much stronger effect to the irradiance than altitude and latitude based on the observations at Lhasa and Nagchu. Note the modeled yearly radiant exposures for clear day conditions at these sites are simulated by estimating a typical summer day amount of water vapour scaled according to altitude. The yearly radiant exposure is also modeled with no water vapour input. Then the solar irradiance increased about 11%, which means that 11% of energy would be absorbed by water vapour in Tibet during summer time.

In comparison to Figure 4.2, Figure 4.14 displays the modeled irradiance sunshine hours at the TOA for Lhasa and Nagchu.

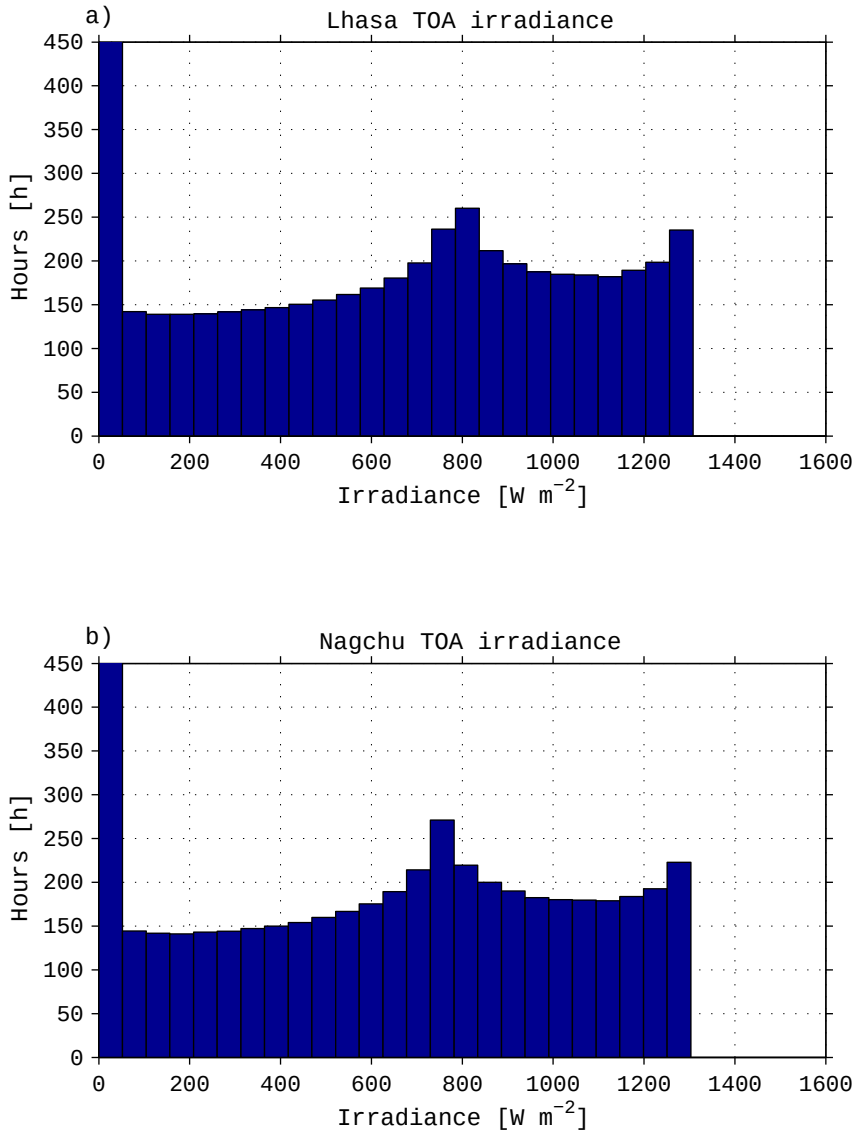

Figure 4.14: Modeled TOA irradiance levels and corresponding sunshine hours in one year at Lhasa (a) and Nagchu (b). (The first bins in (a) and (b) is also cut, the cut values are 4487 hours in (a) and 4488 hours in (b), these long period of time is caused by night time measurements).

4.4 Sensitivity study of Tibetan atmosphere

Xia et al. (2008) concluded that the AOD over the Tibetan Plateau shows distinct seasonal variations. Based on the conclusion of this paper (Xia et al., 2008), a sensitivity study is performed by varying the AOD and the Cloud Optical Depth (COD) over the Tibetan Plateau to understand the impact of aerosols and clouds on the solar irradiance. The AOD varies a lot during a year in Tibet, caused also by the burning of juniper wood and leaves for religious purposes. The AOD varies from 0.11 - 0.27 at 580 nm on the Ti-

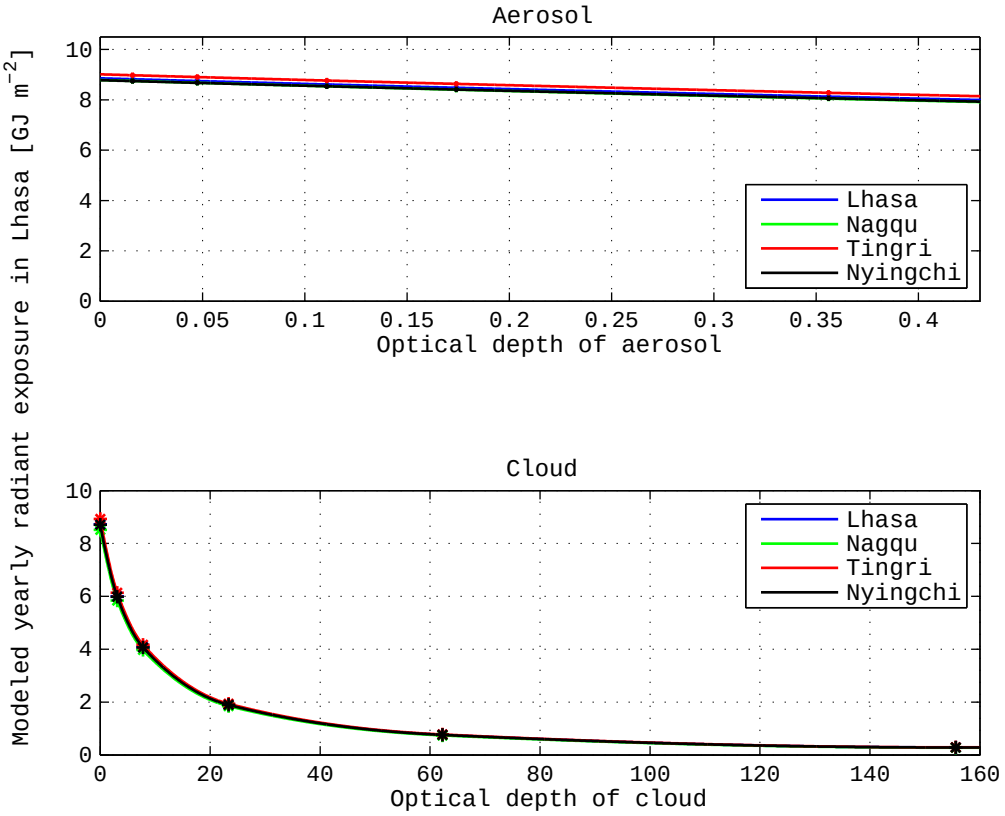

Figure 4.15: Sensitivity study for Lhasa, Nagchu, Tingri, and Nyingchi.

betan Plateau from winter to spring (Xia et al., 2008). As can be seen in the upper panel of Figure 4.15, this AOD fluctuation reduces the corresponding yearly radiant exposure from 3% to 6% for all four sites in Tibet. This influence is not very significant compared to the reduction caused by clouds. When the COD is increased from 0 (clear sky) to 22 (heavily overcast sky), the yearly radiant exposure decreases by about 75%. Note that at a COD of 4.0, the solar disk can barely be seen.

Our sensitivity study was also conducted for a summer atmosphere, with a water vapour absorption of about 11%. However, in autumn or winter time, when there is little water vapour absorption, the influence of the AOD and COD on the yearly radiant exposure is similar to that shown in Figure 4.15.

Chapter 5

Conclusion

Four sites in Tibet have been chosen for measurements of the solar irradiance. The measurements indicate a unique wealth of solar energy resources on the Tibetan Plateau, with irradiance values reaching 1300 W m^{-2}, which are comparable with the high irradiance values at TOA (1300 W m^{-2}). A small portion of the irradiance values even exceeds the maximum TOA irradiance. This phenomenon is caused by irradiance measurements under a very clear sky with only a few clouds close to but not obstructing the line of sight. The daily radiant exposure shows seasonal variation. For a clear winter day, the daily radiant exposure is about 54 % less than for a clear mid summer day. Tingri has the best solar energy resource of all four sites and Nyingchi has the lowest. Lhasa has a richer solar energy resource compared to Nagchu.

Within the time frame of a year, Lhasa has a higher yearly radiant exposure (7.6 GJ m^{-2}) than Nagchu (6.8 GJ m^{-2}). For the typical light-electricity transformation efficiency of 16%, about 5.3 km^2 and 5.9 km^2 of horizontal solar panels are needed to cover the yearly power consumption of the Lhasa prefecture. These two areas are obtained using measured yearly radiant exposures of 7.6 and 6.8 GJ m^{-2}, respectively.

Spectral transmittances are computed applying the radiative transfer model AccuRT. The atmosphere above the two sites in Tibet is much more transparent than above the sites in mainland China. This is another evidence of the rich solar energy resources on the Tibetan Plateau, which is very promising for PV system industry. The solar energy resources on the Tibetan Plateau are affected by weather, latitude and altitude. AccuRT is used to quantify the influence of these factors.

Furthermore, modeled yearly radiant exposures are compared for the same height and the same latitude in all of the four sites. A variation of 3° in latitude accounts for a change of 2% (0.2 GJ m^{-2}) of the yearly radiant exposure, and an altitude variation of 1500 meter also changes the yearly radiant exposure by 2%. Clouds and aerosols were found to affect the yearly radiant exposure by 15% (1.3 GJ m^{-2}) variation in Lhasa and 23% (2.0 GJ m^{-2}) in Nagchu. Therefore, weather has a more significant impact on the solar energy resources than latitude and altitude. Latitude differences have a similar influence as altitude differences on the solar energy resources among the four sites in Tibet.

The yearly radiant exposure is reduced by aerosols by 3% to 6% in a typical AOD variation range in Tibet (0.17 - 0.27 at 580 nm). Comparing actual weather with clear day conditions, the yearly amount of solar energy increases from 7.6 to 8.9 GJ m^{-2} in Lhasa

and from 6.8 to 8.8 GJ m^{-2} in Nagchu.

In this thesis, four sites in Tibet were chosen for irradiance data collection. As future work, it would be useful to conduct measurements in Tingri for at least one complete year, and also try to find other sites which may have even richer solar resources than Tingri. Also, it would be interesting to study what effect the orientation of the solar panel has on the amount of captured light and, hence, on the electricity production. This type of investigation can be initiated by modeling the angular distributions of radiance coming from all directions. In particular, it is useful for sites having high surface albedos to capture more light by solar panels.

The spectra discussed in subsection 4.2.2 were only detected during one day in Tibet and mainland China. The atmospheric properties such as the aerosol sizes and water vapour amount are in general varying with time. In the future, investigation of long term atmospheric properties in Tibet would be very interesting and important for assessment of the future solar energy potential on the Tibetan plateau.

Nomenclature

AccuRT	Accurate Radiative Transfer model
AMF	Aerosol Modification Factor
AOD	Aerosol Optical Depth
BC	Black carbon
CMF	Cloud Modification Factor
CNES	Centre National d'Etudes Spatiales
COD	Cloud Optical Depth
FWHM	Full Width Half Maximum
IOPs	Inherent Optical Properties
MPE	Mean Percentage Error
NILU	Norwegian Institute for Air Research
NPP	Net Primary Productivity
PV	Photovoltaic
RMSE	Root Mean Square Error
RTE	Radiative Transfer Equation
SZA	Solar Zenith Angle
TOA	Top of Atmosphere
UTC	Universal Time Coordinated
YAMF	Yearly averaged Aerosol Modification Factor
YCMF	Yearly averaged Cloud Modification Factor

Bibliography

Instruction Manual, Technical report, Kipp & Zonen, 2013.

Antón, M., a. a. Piedehierro, L. Alados-Arboledas, E. Wolfran, and F. J. Olmo, Extreme ultraviolet index due to broken clouds at a midlatitude site, Granada (southeastern Spain), *Atmospheric Research*, *118*, 10–14, 2012.

Badescu, V., *Modeling Solar Radiation at the Earth ' s Surface*, edited by V. Badescu. Springer, 2008.

Dahlback, A., N. Gelsor, J. J. Stamnes, and Y. Gjessing, UV measurements in the 3000-5000 m altitude region in Tibet, *Journal of Geophysical Research: Atmospheres*, *112* **(9)**, 2007.

Gao, Q., Y. Li, Y. Wan, X. Qin, W. Jiangcun, and Y. Liu, Dynamics of alpine grassland NPP and its response to climate change in Northern Tibet, *Climatic Change*, *97* **(3-4)**, 515–528, 2009.

Gorshelev, V., A. Serdyuchenko, M. Weber, W. Chehade, and J. P. Burrows, High spectral resolution ozone absorption cross-sections – Part 1: Measurements, data analysis and comparison with previous measurements around 293 K, *Atmospheric Measurement Techniques*, *7* **(2)**, 609–624, 2014.

Hamre, B., S. Stamnes, J. J. Stamnes, and K. Stamnes. 2014. AccuRT: A Versatile Tool for Radiative Transfer in Coupled Media like Atmosphere-Ocean Systems. in *Ocean Optics XXII,* , Portland, ME, USA.

Henyey, L., and J. Greenstein, Diffuse radiation in the galaxy, *The Astrophysical Journal*, 1941.

Jaccard, M., *Sustainable Fossil Fuels: The Unusual Suspect in the Quest for Clean and Enduring Energy*. Cambridge University Press, 2006.

Kang, S., P. Mayewski, D. Qin, Y. Yan, S. Hou, D. Zhang, J. Ren, and K. Kruetz, Glacio-chemical records from a Mt. Everest ice core: relationship to atmospheric circulation over Asia, *Atmospheric Environment*, *36* **(21)**, 3351–3361, jul, 2002.

Lewis, Nathan, and Nocera, D. G., Powering the planet: Chemical challenges in solar energy utilization, *Proceedings of the National Academy of Sciences*, *103* **(43)**, 15729—-15735, 2006.

Li, H., W. Ma, Y. Lian, X. Wang, and L. Zhao, Global solar radiation estimation with sunshine duration in Tibet, China, *Renewable Energy*, *36* **(11)**, 3141–3145, 2011.

Liu, J. D., J. M. Liu, H. W. Linderholm, D. L. Chen, Q. Yu, D. R. Wu, and S. Haginoya, Observation and calculation of the solar radiation on the Tibetan Plateau, *Energy Conversion and Management*, *57*, 23–32, 2012.

Liu, X., and B. Chen, Climatic Warming In The Tibetan Plateau During Recent Decades, *International Journal of ClimatologyClimatology*, *20*, 1729–1742, 2000.

Manabe, S., and T. Terpstra, The effects of mountains on the general circulation of the atmosphere as identified by numerical experiments, *Journal of the Atmospheric Sciences*, 1974.

Moosmüller, H., R. Chakrabarty, and W. Arnott, Aerosol light absorption and its measurement: A review, *Journal of Quantitative Spectroscopy and Radiative Transfer*, *110* **(11)**, 844–878, jul, 2009.

Narbel, P., J. P. Hansen, and J. R. Lien, *Energy Technologies and Economics*. Springer, 2014.

Norsang, G., L. Kocbach, W. Tsoja, J. J. Stamnes, A. Dahlback, and P. Nema, Ground-based measurements and modeling of solar UV-B radiation in Lhasa, Tibet, *Atmospheric Environment*, *43* **(8)**, 1498–1502, 2009.

Norsang, G., Y.-C. Chen, N. Pingcuo, A. Dahlback, Ø. Frette, B. Kjeldstad, B. Hamre, K. Stamnes, and J. J. Stamnes, Comparison of ground-based measurements of solar UV radiation at four sites on the Tibetan Plateau, *Applied Optics*, *53* **(4)**, 736, jan, 2014.

Ren, P. B. C., F. Sigernes, and Y. Gjessing, Ground-based measurements of solar ultraviolet radiation in Tibet: Preliminary results, *Geophysical Research Letters*, *24* **(11)**, 1359–1362, 1997.

Stamnes, K., and J. Stamnes, *Radiative Transfer in Coupled Environmental Systems: An Introduction to Forward and Inverse Modeling*. John Wiley & Sons, 2015.

Suehrcke, H., and P. McCormick, Solar radiation utilizability, *Solar Energy*, *43* **(6)**, 339–345, 1989.

Tang, W., K. Yang, J. He, and J. Qin, Quality control and estimation of global solar radiation in China, *Solar Energy*, *84* **(3)**, 466–475, 2010.

Thomas, G. E., and K. Stamnes, *Radiative Transfer in the Atmosphere and Ocean*. Cambridge University Press, 1999.

Wang, Q., and H. N. Qiu, Situation and outlook of solar energy utilization in Tibet, China, *Renewable and Sustainable Energy Reviews*, *13* **(8)**, 2181–2186, 2009.

Xia, X., P. Wang, Y. Wang, Z. Li, J. Xin, J. Liu, and H. Chen, Aerosol optical depth over the Tibetan Plateau and its relation to aerosols over the Taklimakan Desert, *Geophysical Research Letters*, *35* **(16)**, 1–5, 2008.

Yang, K., T. Koike, and B. Ye, Improving estimation of hourly, daily, and monthly solar radiation by importing global data sets, *Agricultural and Forest Meteorology*, 2006.

Zhisheng, A., J. Kutzbach, W. Prell, and S. Porter, Evolution of Asian monsoons and phased uplift of the Himalaya–Tibetan plateau since Late Miocene times, *nature*, 2001.